

Micro-engineered first wall tungsten armor for high average power laser fusion energy systems

Shahram Sharafat ^{*}, Nasr M. Ghoniem, Michael Anderson, Brian Williams, Jake Blanchard, Lance Snead, The HAPL Team

Mechanical and Aerospace Engineering Department, University of California Los Angeles, 46-127A Engr. IV, Los Angeles, CA 90095-1597, USA

Abstract

The high average power laser program is developing an inertial fusion energy demonstration power reactor with a solid first wall chamber. The first wall (FW) will be subject to high energy density radiation and high doses of high energy helium implantation. Tungsten has been identified as the candidate material for a FW armor. The fundamental concern is long term thermo-mechanical survivability of the armor against the effects of high temperature pulsed operation and exfoliation due to the retention of implanted helium. Even if a solid tungsten armor coating would survive the high temperature cyclic operation with minimal failure, the high helium implantation and retention would result in unacceptable material loss rates. Micro-engineered materials, such as castellated structures, plasma sprayed nano-porous coatings and refractory foams are suggested as a first wall armor material to address these fundamental concerns. A micro-engineered FW armor would have to be designed with specific geometric features that tolerate high cyclic heating loads and recycle most of the implanted helium without any significant failure. Micro-engineered materials are briefly reviewed. In particular, plasma-sprayed nano-porous tungsten and tungsten foams are assessed for their potential to accommodate inertial fusion specific loads. Tests show that nano-porous plasma spray coatings can be manufactured with high permeability to helium gas, while retaining relatively high thermal conductivities. Tungsten foams were shown to be able to overcome thermo-mechanical loads by cell rotation and deformation. Helium implantation tests have shown, that pulsed implantation and heating releases significant levels of implanted helium. Helium implantation and release from tungsten was modeled using an expanded kinetic rate theory, to include the effects of pulsed implantations and thermal cycles. Although, significant challenges remain micro-engineered materials are shown to constitute potential candidate FW armor materials.

© 2005 Elsevier B.V. All rights reserved.

1. Introduction

The high average power laser (HAPL) program is a coordinated effort to develop laser inertial fusion

energy [1]. The first stage of the HAPL program will be an engineering test facility (ETF) prior to development of the HAPL demonstration power reactor. The HAPL program is pursuing the development of a solid first wall (FW) chamber.

Following the implosion of the DT pellet, X-rays, neutrons, and charged particles arrive at the first wall (FW) within about 3 μ s in succession of each

^{*} Corresponding author. Tel.: +1 310 794 5990; fax: +1 310 206 4830.

E-mail address: shahrams@ucla.edu (S. Sharafat).

other. Key requirements of a successful dry-wall concept are high-temperature capability, ability to withstand cyclic thermo-mechanical stresses, and recycling of implanted charged particles. A dry wall must also withstand erosion caused by surface roughening, chemical and ion sputtering, and vaporization. Another challenge for a solid FW is the interaction of high-energy helium ions with the wall material. High energy helium ions can be implanted several micrometers deep into a solid material and high helium implantation rates can result in blistering and exfoliation of the FW material.

To mitigate the effects of high temperature pulses and high energy ion implantation, a FW protection scheme is essential for a reliable solid first wall. Separation of the first wall functions into armor and a support structure allows some flexibility in FW development. The joining integrity between the armor and substrate becomes a critical issue for composite FW concepts [2]. High temperature materials, such as carbon have been considered as a candidate FW armor material. Concerns linked with high carbon erosion rates, tritium retention at low temperatures, and radiation enhanced sublimation necessitate development of other FW armor concepts. Refractory metals, such as tungsten are an attractive option because they offer high temperature capabilities, relatively high and predictable thermal conductivities, good sputtering erosion resistance, and near zero tritium retention [3–5]. Allowable erosion rates are extremely stringent and limited to less than 0.02 μm per shot for a tungsten armored FW of the HAPL engineering test facility (ETF).

Helium implantation rates in the FW are estimated to be very large. A month of ETF operation would result in helium implantation equivalent to the number density of solid tungsten. Helium is insoluble in metals and therefore implanted helium ions can migrate rapidly through the host lattice structure until they either leave the metal through free surfaces or are trapped inside lattice imperfections. During implantation helium ions create lattice damage, which provide trapping sites for the helium. The trapped helium coalesces into bubbles, which tend to grow with continued helium implantation until blistering of the armor material occurs. However, cyclic heating (>2000 °C) of implanted helium in tungsten has been shown to reduce the amount of trapped helium [6]. Release of implanted helium is critical for a viable solid FW armor material.

The key FW armor issues can be categorized as:

- (1) Bonding or joining of armor to the FW structural material;
- (2) Erosion due to roughening, sputtering, and vaporization;
- (3) Material response to high helium implantation rates;
- (4) Thermo-mechanical response due to X-ray, proton, and ion energy deposition;
- (5) Macroscopic failure caused by high transient thermal stresses;
- (6) Tritium release and effects on mechanical properties;
- (7) Degradation of material properties under cyclic IFE conditions.

The dry-wall concept depends on a FW protection scheme that successfully addresses all of these issues. We propose here the concept of micro-engineered armor structures to mitigate several of the detrimental effects of incident photon and particles. Micro-engineered armors are based on the concept of geometrically tailoring the structure to provide structural flexibility to accommodate effects of incident radiation, particles, and thermal stress cycles. Recycling of implanted ions, in particular helium could be assisted by micro-engineered structures that contain large amounts of helium sinks, such as internal pores or open surface areas. In the following section, several candidate micro-engineered concepts are introduced. Thermal management of a pulsed heat load and behavior of implanted helium ions in such engineered tungsten armor is then covered. Based on the preliminary assessment of candidate micro-engineered concepts, suggestions for improving and optimization of the micro-engineered armor are outlined.

2. Micro-engineered armor concepts

Extrinsic wall protection schemes can be broadly classified into three categories: (1) gas protection, where significant portions of the X-ray and ion energies are absorbed in a chamber background gas, and then re-radiated over a longer time interval to the FW structure, (2) liquid coolant protection, where the shallow energy deposition of X-rays and ions is prevented from interacting with the FW structure by a flowing sacrificial layer of coolant/breeder liquids (Li or FLiBe), (3) magnetic diversion of ion energy from the first wall by compressing the

expanding ion plasma against a magnetic field, thus drastically reducing the deposited ion energy in FW structures. Instead of the extrinsic wall protection systems provided by gas, liquid, or magnetic media, we suggest micro-structure engineered (micro-engineered) metallic armor, which would be bonded to the FW structure. A micro-engineered armor would have features designed to mitigate the effects of high heat and particle loads.

Micro-engineered features are designed to add significant internal and/or external surface area to the structure. These micro-engineered features would manage the loads over larger areas and deeper inside the structure. In essence, micro-engineered features would accommodate loads quasi-volumetrically, rather than relying only on the top surface layers.

For IFE applications, micro-engineered structures would have geometric features with character-

istic length scales of microns or even sub-microns to accommodate helium release. Examples of micro-engineered structures used for other applications are (1) micro-machined (MEMS-type) structures, (2) plasma-sprayed coatings, (3) foams, and (4) velvet or ‘fiber carpets’. Fig. 1 gives examples of several micro-engineered materials and components: an etched silicon substrate with 200 μm deep \times 200 μm wide channels [7]; a helium-ion implantation pre-processed tungsten surface [8], a carbon fiber carpeted substrate [9]; and a macro-processed castellated tungsten brush limiter (12 cm \times 8 cm) [12]. Fig. 2 shows an example of a nano-porous vacuum plasma sprayed tungsten coating [10] and Fig. 3 shows examples of open cell foam materials.

Electron beam heating experiments have demonstrated to improve thermal performance of a micro-engineered tungsten coating compared with bulk tungsten. In a recent MFE disruption simulation

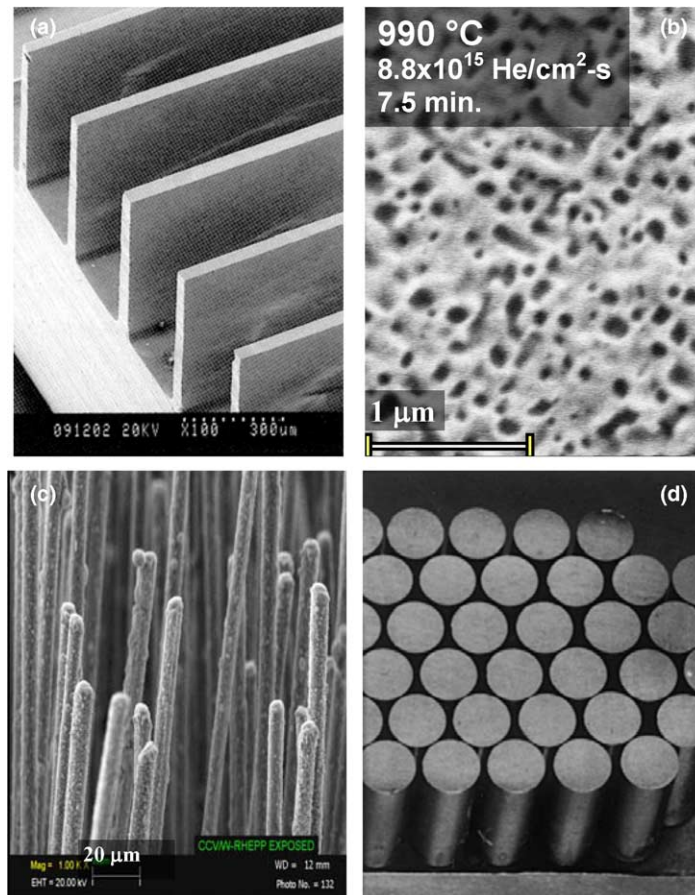


Fig. 1. Examples of micro-engineered structures: etched silicon wafer (a) [7], and helium ion implantation processed tungsten surface (b) [8], a fiber-carpet (c) [9], and a tungsten-brush limiter (d) [3].

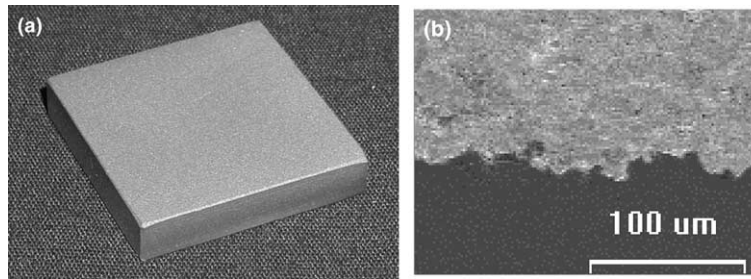


Fig. 2. (a) Photograph showing a VPS deposited nano-porous W deposit on a 25 mm × 25 mm × 5 mm steel coupon, (b) SEM backscattered image showing a cross-sectional view of a nano-porous W deposit on a steel substrate [10].

experiment, both sintered (bulk) and plasma sprayed (micro-engineered) tungsten coatings were exposed to high energy density (2.3 MJ m^{-2}) electron beam pulses [11]. The plasma sprayed tungsten coating experienced higher surface temperatures,

because of reduced thermal conductivity compared with sintered tungsten. However, under identical radiation conditions, the plasma sprayed tungsten did not develop any cracks, while the sintered tungsten coating showed an intense network of cracks

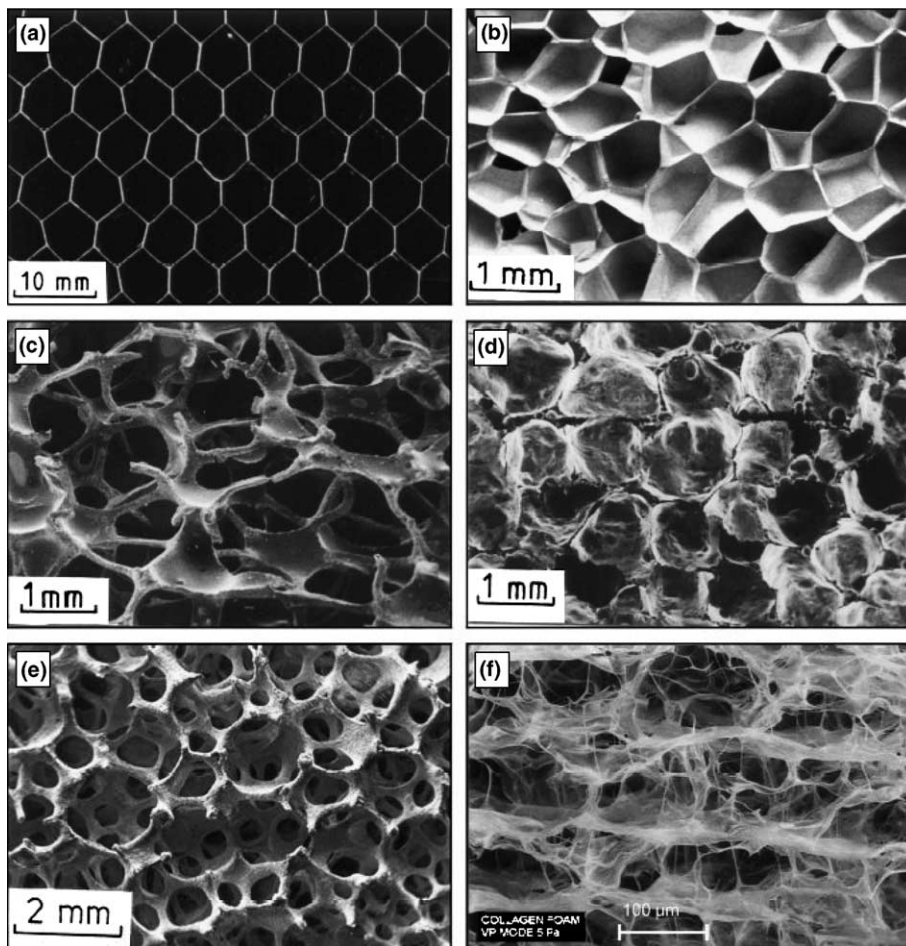


Fig. 3. Engineered cellular materials: (a) Aluminum honeycomb, (b) closed-cell polyethylene foam, (c) open-cell nickel foam, (d) closed-cell glass foam, (e) open-cell zirconia foam, and (f) collagen-based porous scaffold used in tissue engineering [18].

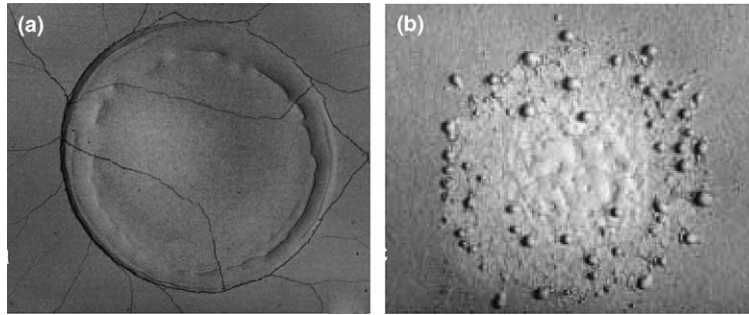


Fig. 4. Electron beam disruption simulation tests, energy density = 2.3 MJ/m^{-2} , pulse duration 1.8 ms; (a) sintered tungsten, $T_0 = 20 \text{ }^\circ\text{C}$, $n = 10$ pulses, (b) plasma sprayed tungsten, $T_0 = 20 \text{ }^\circ\text{C}$, $n = 5$ pulses [11].

(Fig. 4). The sintered tungsten showed the formation of a deep crater, while on the surface of the plasma sprayed tungsten only the formation of spherical tungsten particles of 100–200 μm in diameter could be seen.

2.1. Castellated armor

The fundamental idea behind castellated structures is to minimize thermal stresses by reducing surface expansion constraints. A large and flat surface is ‘broken’ up into smaller sections, which are free to expand independently of each other, thus reducing the total stresses of an otherwise single large flat surface. An example is the macro-castellated tungsten brush limiter, which was exposed to TEXTOR plasma [12–15]. At an incident power of $35\text{--}40 \text{ MW m}^{-2}$ the castellated brush limiter showed superior mechanical behavior compared to a solid tungsten limiters. Hirai et al. concluded that thermally induced surface stresses caused by the temperature gradients were reduced significantly, which helped in preventing crack propagation [12].

Another example of a macro-castellated structure is the US/Boeing tungsten brush structure, which was made by low temperature ($450\text{--}550 \text{ }^\circ\text{C}$) diffusion bonding of small (1.58–3.16 mm diameter) tungsten welding electrodes to soft copper [3] (see Fig. 1(d)). Other castellated tungsten divertor/limiter designs have been tested and shown to perform excellent in cyclic thermal response tests at up to 30 MW/m^2 [13].

Depending on the characteristic dimensions of the castellated structure, various manufacturing techniques can be employed, ranging from precision cutting ($\sim\text{mm}$ scale) to using semiconductor-based plasma etching tools that are used to manufacture MEMS (micro-electro mechanical systems).

2.2. Plasma sprayed armor

Another possible method to micro-engineer FW W-armor with controlled micro-structure is by plasma spray (PS) processing. This technology has been very successful in developing coatings and protective surface treatments, especially with materials that have very high melting points (e.g. refractory metals and ceramics). Because fine powder is melted by plasma heating, and then re-solidified on substrates, great flexibility can be attained in the micro-structure of the final armor. For example, the density and the shape of individual lamella can be controlled by adjustments in the powder feed rate, plasma power, and substrate cooling rate.

One of the key problems that must be dealt with is the high thermal transient in the FW following the pellet implosion, and the associated high temperature and thermal stress. The flexibility gained by a tailored, partially porous plasma spray W-armor can mitigate the effects of thermal stress cycles. Plasma Processes Inc. (PPI) in partnership with UCSD is developing engineered tungsten armor using advanced vacuum plasma spray (VPS) techniques [10].

The engineered tungsten armor is being developed to incorporate a short transport path for helium to migrate back to the armor surface. The method is based on plasma processing nano-sized W-feed powder, to produce porous tungsten coatings on ferritic steel substrates. By controlling the feed rate and heat input to the particles, deposits with nano-sized porosities have been produced by VPS techniques. Fig. 5 shows TEM micrographs of such nano-porous structures produced by PPI. Preliminary testing of the engineered tungsten armor’s porous layer has shown the pores to be interconnected and permeable to helium gas. Both

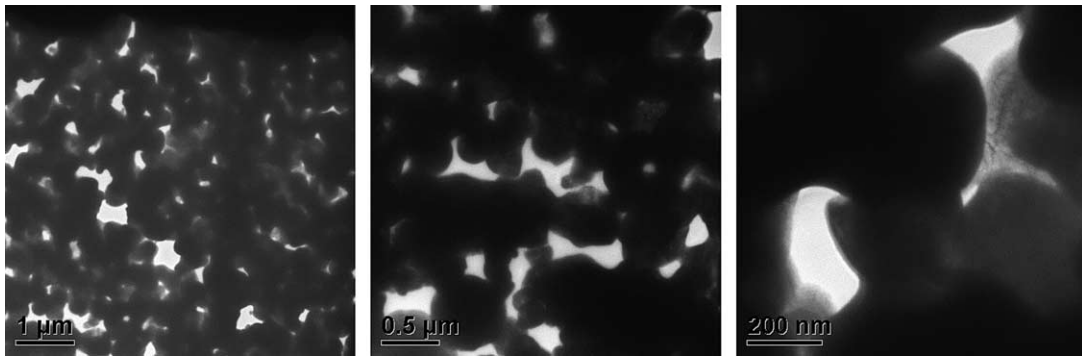


Fig. 5. TEM images of vacuum plasma spray deposited nano-porous tungsten deposits [10].

Table 1

Results of He permeability tests of nano-porous and high-density VPS tungsten deposits [10]

Sample	Q (Torr cm ³ /s)	d (cm)	A (cm ²)	P_2 (Torr)	P_1 (Torr)	K (m ² /s)
Nano-porous W-HfC	8.6×10^{-4}	0.036	0.32	4.3×10^{-3}	1.7×10^{-3}	3.8×10^{-6}
Nano-porous W	1.5×10^{-3}	0.038	0.32	4.7×10^{-3}	1.6×10^{-3}	5.7×10^{-6}
Nano-porous W	2.7×10^{-4}	0.058	0.32	4.1×10^{-3}	1.6×10^{-3}	2.1×10^{-6}
Dense W	$\ll 10^{-6}$	0.064	0.32	$>10^{-2}$	1.6×10^{-3}	$\ll 10^{-9}$
Dense W	$\ll 10^{-6}$	0.038	0.32	$>10^{-2}$	1.6×10^{-3}	$\ll 10^{-9}$
Dense W	3.7×10^{-5}	0.130	0.32	5.3×10^{-2}	1.4×10^{-3}	2.9×10^{-8}

nano-porous and dense tungsten deposits were tested. Nano-porous samples were tested in the as-sprayed condition. The results of the He permeability tests are shown in Table 1. The pressure of the He inlet side was maintained in the 10^{-3} Torr range. In this pressure range, He leak rates between 2.7×10^{-4} to 1.5×10^{-3} Torr cm³/s were measured for the nano-porous tungsten coatings. The permeability of the dense tungsten deposits ranged between 2.1 and 5.7×10^{-6} m²/s.

At UCLA, two hollow-cathode DC-plasmatrons are currently in operation, which can be used in tandem with a vortex generator capable of running at 300 kW at full power. Arata et al. [16], developed a hollow-cathode DC-plasmatron in tandem with a vortex generator. The special feature of this device is the ability to inject powder axially into the plasma beam through a central hole in the cathode. The axial-feeding scheme supplies extremely fine powder along the axis of the plasma plume without distorting the plasma flame. Because the powder-feed gas is introduced into the gun as part of the plasma forming gas, the plasma plume is not cooled by any externally injected gases. To minimize tungsten oxidation during the spray process, the test chamber is evacuated and a shroud filler gas is used. Argon is

used as both the working gas for the plasma and as the carrier gas for the powder.

Fig. 6 shows the optical micrographs of two tungsten coatings produced using the UCLA plasma processing facility [17]: (a) thick (~ 180 μ m) coating and (b) thin (~ 70 μ m) coating. Examination of the thick coating revealed that the tungsten coating close to the steel surface underwent a substantial amount of melting, thus forming a dense W-layer. However, closer to the free surface re-melting did not occur, which resulted in a more loosely packed W-layer containing discernable single W-splats. This process resulted in depth-dependent coating densities. The Vickers hardness along the cross-section was measured near and far from the substrate-coating interface. Near the surface the Vicker's hardness (H_V) was measured to be around 380, while near the substrate it dropped to about 330. X-ray diffraction measurements of the coatings showed strong tungsten peaks, indicating the presence of relatively pure tungsten phases.

These functionally graded plasma-sprayed tungsten coatings with depth dependent porosities are another example of micro-engineered materials, which could help facilitate high helium recycling in IFE FW armor.

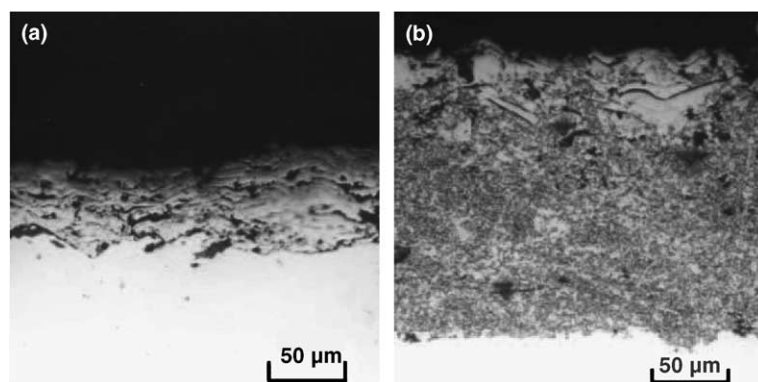


Fig. 6. Optical micrographs showing the cross-section of two W coatings deposited at $L = 40$ mm and $P = 13.5$ kW [17].

2.3. Metallic foam armor

Metallic foams are a relatively new class of material, which are metallic materials of a porous structure with either open cells or closed cells, similar to the structures of sponge or froth, respectively. There are different techniques used for creating foams. Polymers are foamed by introducing gas bubbles into a liquid monomer or hot polymer. The gas is introduced physically by blowing or generated by chemical blowing agents. Another method involves precipitating a polymer as a low-density gel in a fluid, which is then evaporated to produce ultra low-density polymer foams. Carbon foams can be made by graphitizing polymeric foams in a carefully controlled environment. Ceramic foams, such as SiC-foams are produced by using carbon foams as a form. The SiC is then chemically vapor deposited (CVD) onto the carbon ligaments of the carbon foam.

Foaming dramatically extends the range of properties available to engineers, thus creating applications for foams, which cannot easily be filled by fully dense solids. Interest in their applications is increasing rapidly because of unique properties and their ‘multi-functionality’. Metallic foams have excellent rigidity to weight ratios and low densities and are used as structural materials in energy absorbing applications to mitigate the effects of explosions and impacts. Metallic foams are also being used for thermal management, because of their large surface area-to-unit volume ratio (<20000 m²/m³). Other applications included damping materials for noise and vibration absorbers and catalyses [18–23]. High thermal conductivity (180 W/m K) pitch-derived carbon foams have been developed with conductivities approaching that of

solid aluminum (235 W/m K) at about 1/5 the weight [23]. These carbon (graphite) foams are being developed for automotive and electronic heat management systems. Examples of engineered foam materials are shown in Fig. 3.

Mechanical and thermal properties of foams are more sensitive to cell shape than cell size. Foams with equi-axed cell structures have highly isotropic properties, but foams with elongated cells have direction-dependent properties. Honeycomb structures are an example of foam structures with two-dimensionally ordered cells, and where cell walls can share common membranes. Metallic and ceramic foams can be manufactured with randomly oriented cell geometries. The other distinction between different foam architectures is that of closed versus open cell structures. Open cell structures have the distinct topological property of connectivity, which accounts for the unique thermal and mechanical deformation characteristics of such structures. The connectivity of cell faces is the number of faces, which meet at an edge; it is usually three but can be as high as six. The connectivity of cell edges is the number of edges that meet at a node or vertex; usually four in foam. A great variety of cell shapes are possible; however, the cells have to be packed together to fill space in three dimensions. Only a few shapes (five) have been identified to do so: (1) triangular, (2) rhombic, (3) hexagonal prisms, (4) rhombic dodecahedron (a body with 12 diamond-shaped faces), and (5) tetrakaidecahedron (a body with six square and eight hexagonal faces) are true space-filling bodies.

Metallic and ceramic foam structures are predominantly tetrakaidecahedron, for which cell-structure parameters have been identified and listed in Table 2: (1) number of faces, (2) number of edges,

Table 2
Geometric properties of isolated cells [21]

Cell shape	No. of faces	No. of edges	No. of vertices	Cell volume ^a	Surface area	Edge length
Rhombic dodecahedron	12	24	14	$2.79L^3$	$10.58L^2$	$24L$
Tetrahedron	4	6	4	$1/6 L^3$	$1/2 L^2$	L
Tetrahedron	4	6	4	$1/6 L^3$	$1/2 L^2$	L

^a The characteristic length L is defined as the average ligament length (for a 50 ppi foam, the total surface area is of the order of 25000 m²/m³).

(3) number of vertices, (4) cell volume, (5) surface area, and (6) edge length. Most cells have faces with five edges, no matter what the shape of the cell is. Table 2 also lists geometric properties of rhombic dodecahedron cellular structures, another possible candidate foam structure for FW armor applications.

Foam processing techniques affect cell morphology. For example, most polymer foams are made by foaming a liquid polymer. If this is done in a mold, so that the volume expansion causes it to rise in one direction, the cells are generally elongated in the rise direction because of viscous forces. This process results in anisotropic foams with direction dependent properties.

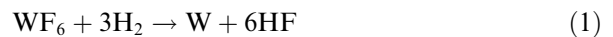
An important property of any cellular solid is its relative density, ρ^*/ρ_s ; where ρ^* is the density of the cellular solid and ρ_s is the density of the solid from which the foam is made. In general, a relative density of 0.3 is the cut-off value between cellular solids and solids containing isolated pores. The porosity of a foam, P , is defined as the fraction of its pore space, or simply, $P = 1 - (\rho^*/\rho_s)$. Foams of various porosities, pore sizes, and densities are now routinely fabricated [23–25].

2.3.1. Metallic foam fabrication

Porous refractory and ceramic coatings are primarily used in the aerospace industry, particularly for rocket engine applications [24]. These materials have withstood tens of hours of exposure to highly corrosive environments at heat flux levels and surface temperatures in excess of 80 MW/m² and 2200 °C, respectively, with minimal erosion. Because tungsten and its alloys are difficult to machine and to assemble into large, complex structures a chemical vapor deposition/infiltration (CVD/CVI) process is employed. The CVD/CVI process is an extremely versatile and relatively inexpensive method of molecular forming of materials and structures that are difficult to create by conventional powder processing and machining. CVD is

used to deposit coatings or to fabricate freestanding structures on removable mandrels, while CVI is used to deposit material inside porous structures such as felts, fiber performs, and foams. The CVD/CVI process has been successfully employed to fabricate a variety of open-cell refractory and ceramic foams.

In a CVD/CVI process, tungsten is deposited at a relatively low temperature of 550 °C through the hydrogen reduction of tungsten hexafluoride (WF₆) under vacuum:



Typical deposition rates for metals of 0.01 in/h are achievable [25]. The benefits of CVD/CVI include the ability to produce deposits of controlled density, thickness, orientation, and composition. Impurity levels are typically less than 0.1%, with densities of 99.9%. In addition, CVD/CVI coatings exhibit the greatest throwing power, or ability to uniformly deposit materials onto/into intricately shaped or textured substrates, thus allowing fabrication of near-net shape parts with geometries that cannot be produced through conventional machining. The greatest benefit of CVD/CVI is probably the fact that numerous materials can be deposited at temperatures that are one-half to one-tenth the melting point of the coating material itself.

Foam fabrication starts with commercially available reticulated polyurethane foams, which is converted to vitreous carbon. Prior to the conversion the polyurethane foam is processed to have the desired cell size and structure of the final foam component. The reticulated vitreous carbon (RVC) foam is then used as a skeletal structure for CVD/CVI of the desired metal or ceramic. The same type of gaseous precursor compound used for CVD processes is used to infiltrate the heated RVC foam substrate. The precursor gas decomposes on the foam ligaments, which results in gradual coating of the foam ligaments with the desired materials. In some cases, after the CVD/CVI deposition process has been

completed, the carbon foam skeleton can be removed through oxidation, leaving behind hollow ligaments. Foams with pore sizes ranging between 3 and 100 ppi (pores per inch) are routinely manufactured. Foams with pore sizes greater than 100 ppi have been fabricated by squeezing the polyurethane foam in one, two, or three dimensions before or during conversion to vitreous carbon [24,25].

An active area of R&D for tungsten foam is the elimination of the carbon core inside the foam ligaments. The carbon inside the tungsten ligaments can interact with the tungsten to form tungsten carbides, such as WC or W₂C. These carbides have lower melting temperatures (2900 °C) than pure tungsten (3460 °C). Recent efforts to eliminate the carbon core prior to W deposition, have succeeded in replacing the carbon core with stable carbides of TaC and HfC cores [26]. These stable carbides will minimize formation of low-melting temperature W-carbides at the interface between the core and the ligament W-coatings of such foams.

3. Design constraints on structural materials for IFE

A detail account of the effects of cyclic energy deposition on armor erosion and armor lifetime for a solid tungsten and carbon-felt based IFE dry FW are given in Ref. [27]. In this section thermo-mechanical effects of the cyclic operation of an IFE environment on micro-engineered candidate materials are briefly outlined.

3.1. Design challenges

The pulsed nature of IFE operations exposes the FW to cyclic thermo-mechanical loads. Component damage resulting from thermo-mechanical fatigue have been identified as a critical issue for the dry-wall HAPL concept. In addition, material properties degrade as a result of neutron, X-ray and ion damage [28,29]. Furthermore, fatigue mechanisms depend on the type and form of the material: high-temperature composites, layered materials, monolithic metallic alloys, plasma sprayed, and foams exhibit different fatigue behavior.

Transient stresses in chamber structures are attributed to a number of sources [28]:

1. Pellet debris momentum;
2. Elastic waves resulting from material ablation, if any;

3. Thermo-elastic waves resulting from the rapid expansion of a thin surface layers;
4. Elastic waves generated by the interaction of chamber gas pressure with the structure.

The first two sources are not likely to contribute significantly, but their exact effect is dependent on target design and chamber protection scheme. They are ignored in our present development of the HAPL dry-wall chamber, since no material evaporation can be tolerated. The relative influence of the last two mechanisms can be tailored by adjusting chamber gas pressure and/or diversion of charged particles and pellet debris, but cannot be eliminated. Thermo-mechanical damage, however, is determined by the rate of energy dissipation in the FW/Blanket structure as a result of thermo-elastic and mechanical stress waves.

The exact tradeoff between transient stresses of thermal or mechanical origins (i.e., generated by gas pressure pulses) is dependent on design details. For example, in the PROMETHEUS IFE design [29,30] and in the earlier SOLACE design [31], pressure-induced transient stresses are dominant. Without any detailed structural design of the HAPL chamber, fatigue lifetime determination would be tentative at best. It must therefore be recognized that the issues of chamber mechanical design cannot be isolated from the issues of current material database utilization, and more likely, the need to develop new material structures that can meet mechanical design criteria. In other words, iteration cycles are expected between mechanical design optimization and material development.

3.2. Neutron effects on material degradation

The average displacement damage rate caused by neutron irradiation in the FW of IFE systems is comparable with MFE systems, and is on the order of $\sim 10^{-6}$ dpa/s. The expected average damage rate in a MFE FW steel structure is between 15 and 20 dpa/FPY. The associated helium generation in a MFE steel structure would be about 200–300 He-appm/FPY. However, in HAPL IFE the time averaged damage rate caused by ion implantation in exposed tungsten is estimated to be a factor of 1000 higher ($\sim 10^{-3}$ dpa/s, Table 5). Furthermore, the instantaneous damage rate is typically 6–8 orders of magnitude larger than in MFE. Although MFE relevant average displacement damage rates and He-generation rates are attainable with present

day fission reactors, the large damage rates and helium implantation rates in IFE FW structures are not.

The higher instantaneous damage rate in IFE is expected to promote rate-sensitive micro-structure processes (such as point defect formation and recombination, homogeneous cluster nucleation, etc.), while the short downtime between pulses may have an effect on temperature-sensitive micro-structure processes (e.g. annealing effects on micro-structure kinetics). Limited information exists in the literature for guidance on how to extrapolate fission reactor and ion irradiation effects to these unique conditions of IFE. If one uses fission reactor data on C, SiC and refractories, then we need to establish the extent that the pulsed nature of radiation alters the radiation response of these materials. Some common materials problems with MFE that are worthy of consideration involve very large rates of internal gas generation in both C and SiC based materials. If these materials are to be used for a few years of operation, percent levels of their atoms will transmute into gas (hydrogen and helium). The effects of this type of burnup on properties are not well understood.

SiC is a very brittle material and its engineering into useful composite forms is at its infancy. At low temperatures, neutron radiation results in a considerable degradation of thermal conductivity that limits the surface heat flux, results in internal micro-cracking that reduces the strength, and can lead to differential swelling of the fiber/interface/matrix system that may lead to premature failure. We do not know how the pulsed neutron irradiation rate at 6–7 orders of magnitude higher than fission reactors will affect these phenomena.

Graphite-based materials are not resistant to the damaging effects of neutron irradiation either. Since the early days of fission reactor development, it is well documented that graphitic materials first undergo initial shrinkage with increasing neutron fluence, followed by unstoppable growth and swelling of several tens of percent per dpa (displacement per atom). Recent developments in the field of high-temperature composite materials show that a great deal of ‘materials engineering’ can be done to impart structural properties to these normally non-structural materials. Thus, textile weaving concepts, followed by various methods of matrix infiltration, and materials processing routes can result in superior structural components for severe applications,

such as re-entry vehicle nose cones, rocket engine thrusters and combustion chambers, etc. In addition, we may be able to ‘engineer’ the architecture of such materials to delay the expected neutron induced dimensional instability. But this remains a great challenge.

3.3. Pulsed X-ray and high energy ion effects on surface ablation

The ejection of carbon atoms from the surface layers of graphite under thermal and low energy ion (keV) irradiation is well known. Chemical erosion is important between 600 and 1000 K and shows no particular energy threshold, while radiation enhanced sublimation (RES) dominates in the 1400–2000 K range. While RES has been systematically studied for MFE, carbon surface interaction with the IFE-relevant high-energy ion irradiation is unknown. Results from high temperature, high-energy electron irradiation suggest that IFE conditions will yield greater erosion rates compared with MFE. Experimental and complementary modeling research programs are needed to address the fundamental issues of surface atom removal (e.g. carbon, Si, W, etc.) as a result of the severe non-equilibrium conditions encountered during the short time of X-ray and fast-ion energy deposition.

The fundamental mechanisms of ion interaction with surface and sub-surface atomic layers during fast ion energy deposition are not well understood. Sub-threshold ejection of surface atoms into the chamber is very hard to quantify, because millions of low-energy shots have to be accumulated before such effects can be measured.

3.4. Fatigue and synergistic neutron and thermo-mechanical damage

IFE Direct Drive targets release about 2% of their fusion energy as X-rays, over the span of several nanoseconds. These X-rays heat target-facing surfaces, potentially generating thermal damage, ablation and large impulse loads. Modeling surface response is of fundamental importance to assessing the feasibility of IFE chamber designs, but involves highly complex phenomena including chemical dissociation and ionization, thermal and radiation energy transport, and hydrodynamic response. The predominant mode of failure in IFE structural materials is likely to be fatigue due to the pulsed

nature of the system. Factors, which may affect material fatigue properties in an IFE environment, include neutron irradiation damage and helium and hydrogen embrittlement.

In addition, first wall surface alterations caused by pulsed heating and shock waves can serve as crack initiation sites. The assessment of synergistic neutron and thermo-mechanical damage is very challenging because of its impact on structural reliability and integrity. For example, what are the mechanisms of strength degradation after millions of shots? How can we control the degree of damage under these conditions by materials design methods? How reliable will chamber walls be, and for how long?

Rudimentary lifetime and reliability estimates have been the hallmark of design studies in most cases so far. These have been based on very simplistic data gathering (e.g. the canonical 5% swelling limit). For realistic development of reliable IFE FW structures, it is extremely important to know what determines the actual limit of a component's life.

4. Thermal management

The pulsed nature of the almost instantaneous and high heating of the FW armor poses a significant challenge for thermal management. The X-rays and ions deposit their energy (~ 45 MJ for a 154 MJ target) up to a depth of <10 μm in a solid tungsten armor. The neutron energy (~ 109 MJ) is deposited volumetrically throughout the FW and blanket, with only about 800 MW/cm^3 being deposited in a solid FW tungsten armor. In a 6.5 m radius chamber X-ray photons deposit their energy (2.1 MJ) within a depth of about 0.5 μm in solid tungsten over a 1 ns pulse width. About

125 ns later neutrons deposit about 800 MW/cm^3 for over 5 ns. About 0.1 μs later, the burn ions arrive, depositing about 18.1 MJ to a depth of about 5 μm over a time interval of about 1 μs . Finally, the debris ions deposit about 24.9 MJ within a depth of about 1 μm over a period of about 2 μs . The X-rays and ions deposit their energies very close to the surface, while neutrons heat the armor volumetrically.

The thermal response of solid tungsten and that of tungsten foam armor were analyzed based on the threat spectra. Three-dimensional FEM analyses were performed for both the solid and the foam armor. Although a 1-D model suffices for a thermal analysis of the solid armor, a 3-D model was developed in order to benchmark the 3-D analysis for complex foam structures.

4.1. Particle and radiation threat spectra

In this section, we discuss the anticipated radiation threat spectra [32] impinging on the first wall of the dry-wall IFE chamber in a full-scale fusion power plant. For a detailed description of the threat spectra and energy deposition profiles, please refer to Raffray et al. [33]. The parameters for the IRE (integrated research experiment) and the ETF (engineering test facility) machines are also included to show how close each would come to producing the desired threat spectra. This provides a measure of how useful IRE and ETF would be for materials testing. One of the main goals of the ETF is to provide a test bed for validating IFE materials and component performance. The main characteristics of the threat spectra for the IFE dry wall concepts are summarized in Table 3 and a summary of the temporal structure for threat spectra of a 150 MJ pellet is shown in Table 4 [34].

Table 3
Characteristics of threat spectra for the IFE dry wall concepts [32]

	IRE	ETF	Power plant
Driver energy	0.1 MJ	1–2 MJ	2–4 MJ
Yield	0	50–200 MJ	150–450 MJ
Repetition rate	~ 5 Hz (burst mode)	5–10 Hz (hours at a time)	5–15 Hz
Neutrons	0	$\Phi_{14\text{ MeV}} = 2\text{--}8 \times 10^{11}$ n/cm^2 shot	$\Phi_{14\text{ MeV}} = 5 \times 10^{12}$ n/cm^2 s $\Phi_{\text{fast}} = 9 \times 10^{12}$ n/cm^2 s $\Phi_{\text{Total}} = 10^{13}$ n/cm^2 s
X-rays (per shot)	6 mJ/cm^2	14–56 mJ/cm^2	19–76 mJ/cm^2
Ions (per shot)	2 mJ/cm^2	0.3–1.1 J/cm^2	0.4–1.1 J/cm^2
Gamma-rays	0	0.7–3 Gy/shot	$\sim 10^9$ Gy/y

Table 4

Timing, heating rates, and characteristic penetration depths in solid tungsten for a 6.5 m chamber, 154 MJ target with no chamber gas [34]

Heating source	Arrival time (ns)	Pulse width (ns)	Peak heating rate (W/m ³)	Penetration depth in W (μm)
Photons	0	1	2×10^8	<0.5
Neutrons	125	5	8.2×10^{14}	–
Burn ions	200	800	4.4×10^{14}	<10
Debris ions	1000	2100	2.3×10^{16}	<2

4.2. Material properties and FEM analysis

In its simplest form, the FW structure consists of a thin (less than ~1 mm) solid tungsten layer on top of a low activation oxide dispersion strengthened (ODS) ferritic steel (~1 mm), which is bonded to a low activation ferritic steel (LAFS) substrate (~2 mm). The coolant channels are located at the bottom of the LAFS substrate. For all thermo-mechanical analyses it is assumed that the helium coolant bulk temperature is 400 °C and the heat transfer coefficient is 10000 W/m² K. The high heat transfer coefficient assumes an internal pipe flow with a coolant pressure of 10 MPa, a hydraulic diameter of 1.7 cm, a coolant velocity of 50 m/s, and sand grain level roughness [35]. Material properties used for thermo-mechanical analyses are as follows:

Thermo-mechanical properties of F82H (8–9%Cr reduced activation ferritic–martensitic steel) [36]:

1. Ultimate tensile strength (unirradiated):

$$\sigma_{\text{UTS}} \text{ (MPa)} = 683 - 1.162T + 0.00547T^2 - 1.17 \times 10^{-5}T^3 + 6.24 \times 10^{-9}T^4 \quad (T \text{ in } ^\circ\text{C}).$$

2. Yield strength (unirradiated):

$$\sigma_Y \text{ (MPa)} = 531 - 0.388T + 0.00148T^2 - 2.4 \times 10^{-6}T^3 + 1.45 \times 10^{-10}T^4 \quad (T \text{ in } ^\circ\text{C}).$$

3. Elongation:

ε_{tot} (%), RA are moderate to high in unirradiated and irradiated conditions, ($\varepsilon_{\text{tot}} \sim 8\text{--}10\%$ for $T_{\text{irr}} < 400$ °C).

4. Elastic constants:

$$E \text{ (GPa)} = 233 - 0.558T$$

for $20 < T < 450$ (T in Kelvin),

$$G \text{ (GPa)} = 90.1 - 0.0209T$$

for $20 < T < 450$ (T in Kelvin),

$$\nu = (E/2G) - 1.$$

5. Thermo-physical properties:

$$\alpha_{\text{th}} = 10.4 \text{ ppm}/^\circ\text{C} \quad (20 \text{ } ^\circ\text{C}) \text{ to } 12.4 \text{ ppm}/^\circ\text{C},$$

$$C_p = 0.47 \text{ J/g K} \quad (20 \text{ } ^\circ\text{C}) \text{ to } 0.81 \text{ J/g K} \quad (700 \text{ } ^\circ\text{C}),$$

$$k_{\text{th}} = 33 \text{ W/m K} \quad (20\text{--}700 \text{ } ^\circ\text{C}).$$

Thermo-mechanical properties of W–(5–10%) Re Tungsten [37,39]:

1. Ultimate tensile strength (unirradiated):

$$\sigma_{\text{UTS}} \text{ (MPa)} = 377.9 + 0.03207T - 1.955 \times 10^{-4}T^2 + 5.13 \times 10^{-8}T^3 \quad (T \text{ in } ^\circ\text{C}).$$

2. Yield strength (unirradiated):

$$\sigma_Y \text{ (MPa)} = 94.2 - 0.0214T - 2.12 \times 10^{-6}T^2 - 7.48 \times 10^{-10}T^3 \quad (T \text{ in } ^\circ\text{C}).$$

3. Elongation (annealed):

$$\varepsilon_{\text{tot}} \text{ (%) } = 20.8 + 5.30 \times 10^{-2}T - 2.18 \times 10^{-5}T^2 \quad (500 \text{ } ^\circ\text{C} < T < 2750 \text{ } ^\circ\text{C}).$$

4. Elastic constants:

$$E \text{ (GPa)} = 398 - 0.00231 \times T - 2.72 \times 10^{-5}T^2 \quad (T \text{ in } ^\circ\text{C});$$

$$\text{Pure W: } \nu = 0.279 + 1.09 \times 10^{-5}T \quad (T \text{ in } ^\circ\text{C});$$

$$\text{W–25Re: } \nu = 0.30; \quad (E = 410 \text{ GPa},$$

$$G = 159 \text{ GPa}) \quad (T = 20 \text{ } ^\circ\text{C}).$$

5. Thermophysical properties:

$$\alpha_{\text{th}} \text{ (} 10^{-6}/^\circ\text{C)} = 3.9 + 5.8 \times 10^{-5}T + 5.6 \times 10^{-11}T^2 - 2.0 \times 10^{-14}T^3 \quad (T \text{ in } ^\circ\text{C}),$$

$$C_p \text{ (J/kg K)} = 128 + 0.033T - 3.4 \times 10^{-6}T^2 \quad (T \text{ in } ^\circ\text{C}),$$

$$k_{\text{th}} \text{ (W/m K)} = 174.9274 - 0.1067T + 5.00674 \times 10^{-5}T^2 - 7.83494 \times 10^{-9}T^3 \quad (0 < T < 3500 \text{ } ^\circ\text{C}).$$

4.3. Transient temperatures in tungsten armor

The energy spectra of X-rays and ions from a 154 MJ DD target implosion are given in Table 4. The high energy density of both the X-rays and the ions result in almost instantaneous heating of the FW armor surface layers. Rapid heating of the armor surface sets up high transient temperatures, which are of concern for a number of reasons.

First, we would like to ensure that the surface temperature of the FW tungsten armor does not exceed its melting point (3460 °C for W), and that evaporation rates of armor are kept as low as possible. Second, a rapid rise in surface temperatures can result in significant thermal expansion and stress wave propagation in the armor. Furthermore, high temperatures can result in significant micro-structural changes, such as grain growth, dislocation sub-structure annealing, pore closure, etc. inside the bulk of the armor material. To reduce the possibility of significant micro-structural changes, we will have to be more conservative as not to allow the bulk temperatures to reach more than a prescribed fraction of the melting point; for example 60% of the melting point ($0.6T_{\text{melt}} = 2204 \text{ °C}$ for W) could be an appropriate design limit.

The thermal response of the armor-FW structure to rapid heating of the top surface layers ($<5 \mu\text{m}$) was analyzed using a three-dimensional finite element model (FEM). Material properties listed in Section 4.2 were used. Details of the loading conditions, such as neutron heating, pulse durations, heating rates, and the deposition depth of the X-rays and debris and burn ions are listed in Table 4 [34]. Symmetry boundary conditions were applied

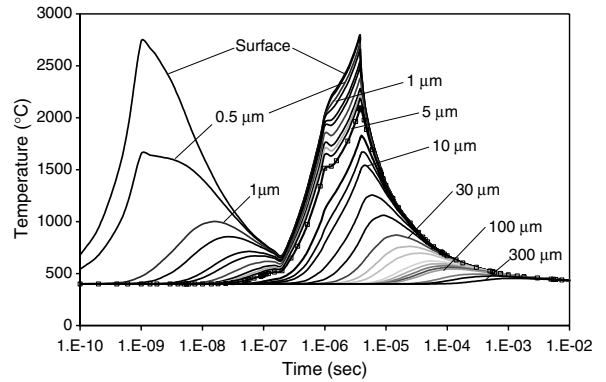


Fig. 7. Transient temperature profiles in a 300 μm -thick solid tungsten armor on top of a 1 mm ODS and 2 mm LAFS composite FW structure during a single 154 MJ target implosion in a 6.5 m radius chamber with no gas protection [38].

to all sides of the 3-D model, except for the heated surface and the cooled back side of the model.

The surface temperature of a solid tungsten reaches a maximum of about 2800 °C (Fig. 7), which is below the melting temperature of tungsten (3400 °C) but above the self-imposed 60% T_{melt} limit. However, beyond a depth of 5 μm from the surface the maximum tungsten armor temperatures stay below the 2200 °C limit. The FE-model was used to investigate an optimum tungsten armor thickness. An optimum armor thickness will keep the surface temperatures below melting (3400 °C), minimize armor-steel interface temperatures ($<550 \text{ °C}$), and keep the armor-steel interface temperature swing during a single pulse as low as possible (30–50 °C).

Fig. 8 shows the results of scoping temperature calculations. For thin tungsten armor coatings

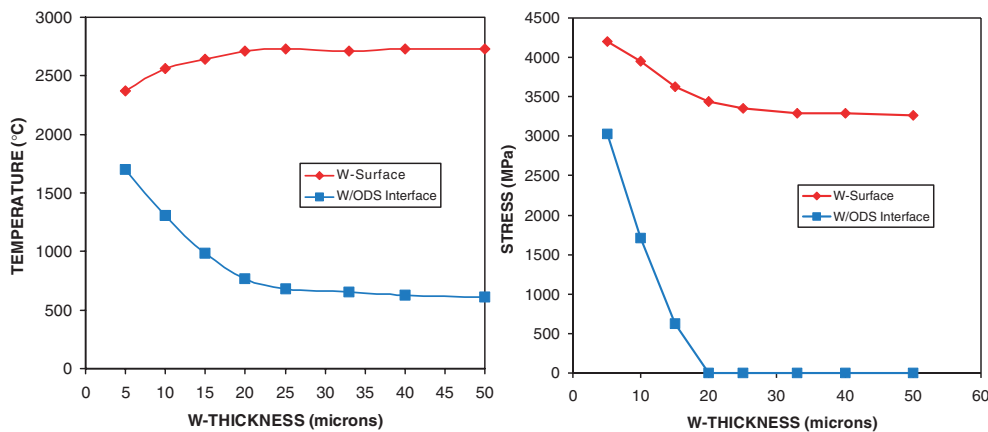


Fig. 8. Maximum W-surface and the W/ODS interface temperatures and stresses as a function of solid tungsten armor thickness on (elastic analysis).

(5 μm) the maximum surface temperature reaches about 2400 $^{\circ}\text{C}$, however the tungsten–steel interface temperatures of around 1700 $^{\circ}\text{C}$ are well above the maximum allowable ODS temperatures (~ 700 $^{\circ}\text{C}$ at 100 MPa). As the tungsten thickness is increased, the heat capacity of the armor increases, resulting in a lowering of the tungsten–steel interface temperature, but at the expense of higher surface temperatures. The tungsten surface temperature increases because of longer conduction path to the cooled steel structure. At a thickness of about 20 μm the tungsten armor asymptotes to a maximum surface temperature of 2800 $^{\circ}\text{C}$ and the tungsten–steel interface temperature reaches the minimum value of about 750 $^{\circ}\text{C}$. This implies that tungsten armor thickness of 20 μm would not be sufficient to protect the main ODS ferritic structure from the high temperature transient at the FW surface. Tungsten thicknesses of the order of about 300 μm are necessary to keep the tungsten–steel interface temperature around the allowable of about 500 $^{\circ}\text{C}$ and to keep the temperature swing below a 50 $^{\circ}\text{C}$ limit (see Fig. 8).

4.4. Thermal response of micro-engineered armor

Of the micro-engineered armor candidate concepts only the plasma sprayed nano-porous tungsten and the tungsten foam have been developed to any significant degree. Thermo-mechanical analysis of plasma-sprayed coatings is a very challenging undertaking; in that plasma sprayed coatings consist of ‘loosely’ bonded re-solidified splats. Elastic properties of plasma sprayed coatings are highly an-isotropic and thus difficult to characterize and/or to measure. Thermal conductivity and density measurements of plasma sprayed coatings can be performed with a high degree of accuracy, but were

not available at the time of writing this paper. An analysis of plasma-sprayed porous tungsten based on simplified property assumptions is described in the companion paper by Raffray et al. [33].

Micro-engineered tungsten foam armor, however consists of dense tungsten ligaments, for which elastic and thermal properties are well established. The thermal response of the tungsten foam structure depends on conduction along ligaments, radiation between hot and cold ligaments, and if present convection on ligament surfaces. Of these processes, we will only consider the conduction along foam ligaments, because there is no convection and re-radiation of absorbed photon energy back into the foam itself is too complex for the scope of these preliminary investigations.

The challenge lies in developing a detailed three-dimensional solid model of the foam for FE analysis. A three-dimensional solid model of a 200 ppi foam structure was created using truncated octahedron Kelvin Cells, which were stacked into a 64 cell matrix ($4 \times 4 \times 4$), with ligament length of 80 μm and thickness of 20 μm . Fig. 9 shows the three-dimensional foam solid model side-by-side with a micrograph of an 80 ppi molybdenum foam. The foam solid model is oriented on top of the steel substrate so that W-foam ligaments intercept all of the incident radiation. Fig. 9 shows a cut section of the W-foam solid model on top of the 3-mm thick FW ODS/LAFS steel substrate. None of the foam parameters have yet been optimized; they serve only to scope the thermo-mechanical response of foam armor.

4.4.1. Loading conditions in foam structures

In open-cell foam structures, the radiation emanating from the micro-explosion is intersected by foam ligament surfaces, which lie in direct line of sight of the incident radiation. The top ligaments

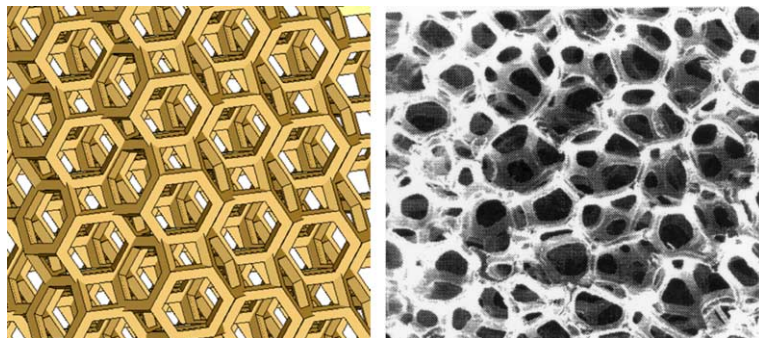


Fig. 9. Rendered three-dimensional solid model (left) of tungsten foam (left) shown next to an optical micrographs of an 80 ppi, 20 vol.% dense CVI Mo foam at 60 \times magnification [25] (right).

are thus fully exposed to incident radiation, while internal ligaments intercept less radiation because of shadowing by above ligaments. Thus, with depth ligaments experience successively reduced loading until finally at the foam/steel interface none of the ligaments receive any direct heating. Large fractions of the heat load are deposited deep inside the foam. In effect, the open cell structure and the shadowing phenomenon results in a ‘quasi-volumetric’ heating in foams compared with that of purely surface heated bulk solids.

To model the quasi-volumetric heating in a foam structure the shadowing of each ligament has to be modeled with great detail. Such a model was generated and the 3-D shadowing was mapped onto individual ligaments. Based on the direct line of sight, successively smaller and smaller portions of deeper lying ligaments were illuminated with the X-ray and ions. In the current 3-D solid foam model, over 90 such surfaces were identified for illumination by X-ray photons and ions (see Fig. 10).

To model the successive loading caused by neutrons, X-rays, burn ions, and debris ions, a detailed volumetric heat load model had to be created. Neutron penetrate the entire structure, X-rays penetrate about 0.5 μm , while burn ions go as deep as 5 μm ,

and debris ions penetrate only up to about 1 μm into solid tungsten. A composite 3-D model was developed, with detailed X-ray, burn-ion, and debris-ion volumes, to allow simulation of the depth and temporal deposition of these three heat loads in a successive fashion. Details of the volumetric heating rates as a function of time and depth for all four constituents are given in Table 4. In all cases the debris ions resulted in the highest temperature rise. Using the detailed 3-D solid foam armor FW model, both ‘quasi-steady-state’ and the transient temperature analyses were performed and are discussed here.

4.5. Quasi-steady-state thermal analysis of W-foam

The ETF is designed to operate at a repetition rate of 5 Hz for an NRL 154 MJ direct drive target. The equivalent average thermal surface loading of the FW armor is estimated to be about 45 MJ/shot, which translates to 0.40 MW/m² surface heat flux on a 6.5 radius chamber FW. Estimates of the steady state temperature distributions in the W-foam structure and the underlying ODS steel structure are shown in Fig. 11. It is apparent that the steady-state temperature profiles in the tungsten ligaments ($T_{\text{max}} = 640\text{ }^{\circ}\text{C}$), the W/ODS interface

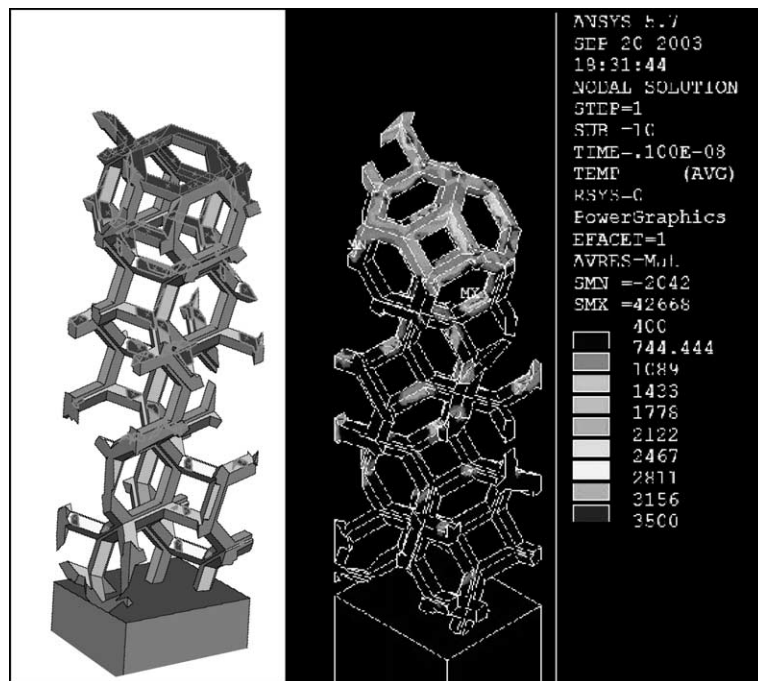


Fig. 10. FEM of a tungsten foam armor on top of steel substrate; sections of ligaments that are in direct line of sight of radiation are illuminated and depicted in a darker shade (left picture) resulting in ‘quasi-volumetric’ heating of foam, i.e., smaller and smaller sections of deeper lying ligaments are heated; temperatures ($^{\circ}\text{C}$) at the end of the X-ray pulse (1 ns) are shown in the right figure.

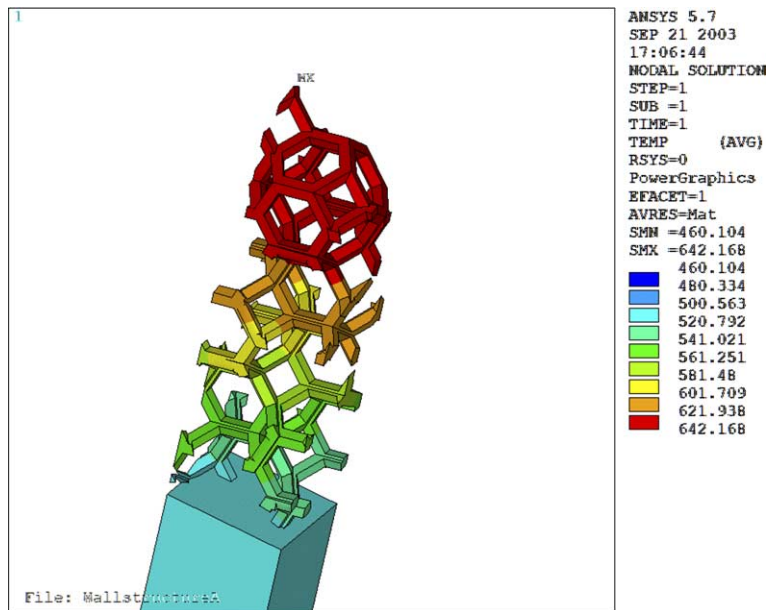


Fig. 11. Steady-state temperature distributions in the W-foam and the ODS steel structure based on 45 MJ per shot (X-ray plus ions), which translates to 0.43 MW/m^2 for a chamber with 6.5 m radius with a repetition rate of 5 Hz.

($T_{\text{max}} = 520 \text{ }^\circ\text{C}$), and the ODS steel ($T = 500 \text{ }^\circ\text{C}$) structure are quite mild. The heat transfer coefficient for the coolant on the steel side was taken to be $10000 \text{ W/m}^2 \text{ K}$, the coolant temperature is assumed to be $400 \text{ }^\circ\text{C}$, and an average tungsten thermal conductivity of 100 W/m K was assumed for the quasi-steady-state calculations.

4.6. Transient thermal analysis of W-foam

The detailed 3-D solid model of W-foam was used for a transient thermal analysis. Temperature dependent material properties, such as thermal conductivity, specific heat, and density were used [36,39]. The first wave of deposited energy is associated with the arrival of the X-ray photons. The rapid energy deposition time (1 ns) results in a very fast temperature rise in the surface of radiation facing foam ligaments. Within about 1 ns, the surfaces of the top ligaments of the foam reach temperatures close to $2900 \text{ }^\circ\text{C}$. The surface temperatures of internal ligaments also rise rapidly, but do not reach the same high levels as the first layer, because of shadowing by upper ligaments resulting in smaller heat-load footprints. For example, the surface of ligaments at a depth of $\sim 1 \mu\text{m}$ reaches a maximum temperature of only $1500 \text{ }^\circ\text{C}$. The reason is the large heat capacity of the adjacent cold ligament mass. It is expected, however that a very

fast elasto-plastic stress wave initiates from the heated ligament surfaces, which runs through the foam structure. This remains to be investigated.

Temperature evolution in the foam is shown in Fig. 12. The sequence of frames represent the end of X-rays (1 ns), after neutrons and start of burn ions (200 ns), middle of burn ions (600 ns), end of burn and start of debris ion (1000 ns), half way into of debris ions (2000 ns), and end of debris ions (3100 ns).

The thermal energy associated with the X-ray pulse decays within about 10 ns, and the foam temperature is restored to almost initial conditions within approximately 100 ns. However, as soon as the temperature of the first few microns of the W-foam decays down to near the steady-state operating range, the arrival of the burn ions at about 200 ns, and the debris ions at about $1 \mu\text{s}$ result in a second temperature rise. The analysis shows that the second temperature rise reaches almost $3000 \text{ }^\circ\text{C}$, which decays to steady-state operating conditions before the arrival of the next pulse.

The maximum temperature of tungsten foam ligaments is almost $200 \text{ }^\circ\text{C}$ higher than the maximum of a solid bulk tungsten coating (Fig. 7). The reason for the higher T_{max} is the presence of sharp 90° edges along the ligaments. Typically, refractory foams have round ligaments with no sharp corners. A three-dimensional foam solid model with round

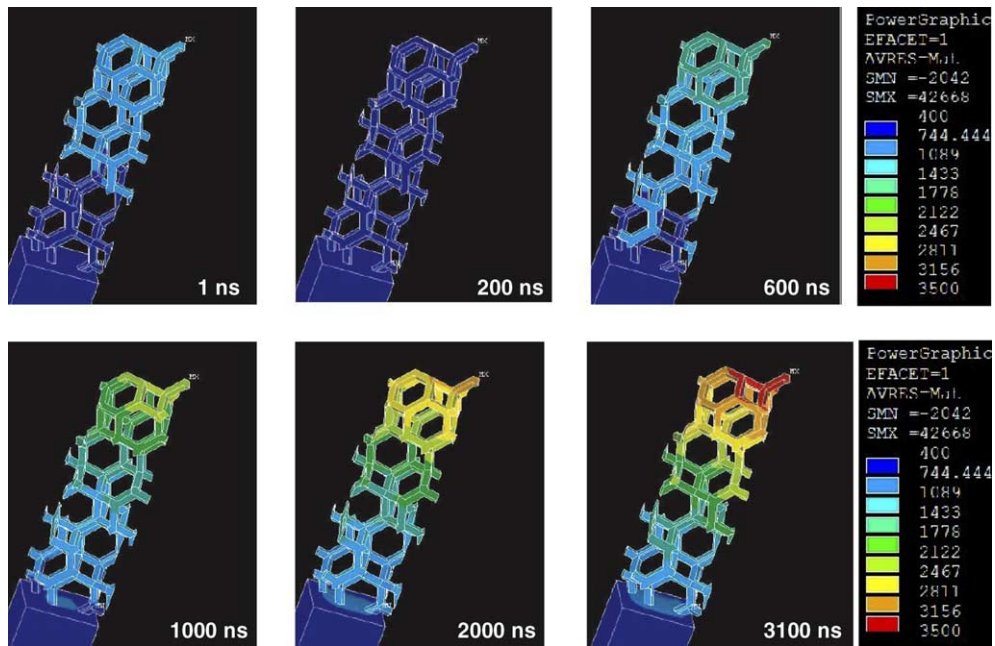


Fig. 12. Temperature ($^{\circ}\text{C}$) evolution of the foam at various times during a single pulse (end of the X-rays (1 ns), neutrons and start of burn ions (200 ns), middle of burn ions (600 ns), end of burn and start of debris ion (1000 ns), half way into of debris ions (2000 ns), and end of debris ions (3100 ns)).

ligament cross-sections would make FEM analysis computationally prohibitive.

5. Thermo-mechanical response of tungsten armor

5.1. Thermal stresses in a solid tungsten armor

The almost instantaneous temperature rise of the top armor surface will result in large temperature gradients that lead to thermal stresses. At the armor substrate interface temperature gradients are small; however differences in material properties can lead to thermal stresses. In both cases, the cyclic nature of the temperature fields can give rise to fatigue damage. A transient thermo-mechanical fatigue analysis is being conducted and results will be reported in future publications.

We report here the results of a rudimentary elastic thermo-mechanical scoping analysis, which is based on a simplified thermo-mechanical model with full in-plane constraint. In-plane thermal stresses are given by:

$$\sigma \approx \frac{\alpha E (T_{\text{av}} - T_s)}{1 - \nu}, \quad (2)$$

where α = thermal expansion coefficient, ν = Poisson's ratio, E = Young's modulus, T_s = interface

or surface temperature, and T_{av} = average temperature. Tungsten surface and the tungsten/ODS interface temperatures were estimated using a 1-D FEM. The effect of armor thickness on thermal stresses was estimated as a function of armor thickness and is depicted in Fig. 8.

Near surface thermal stresses in a 5- μm thick coating could reach large values of 4 GPa and an interface stress of 3 GPa. These stress levels are well beyond allowable limits and would result in instantaneous failure of both the armor surfaces and the interface. As armor thickness increases beyond 20 μm , the interface stresses drop to negligible levels while armor surface stresses asymptote to a 3 GPa value.

A three-dimensional elastic transient thermo-mechanical FEM analysis was made of a 300 μm -thick tungsten armor on the ODS/LAFS (1-mm/2-mm) substrate. Transient heating loads and penetration depths were based on the threat spectra (see Table 4). Lateral constraints were modeled by applying symmetry boundary conditions to all but the top (heated) and the bottom (cooled) surfaces. A snap shot of the thermal stresses at the end of helium implantation is shown in Fig. 13. The top layer of the armor experiences a maximum stress level of about 3.7 GPa, which is comparable with the simplified model results using Eq. (2).

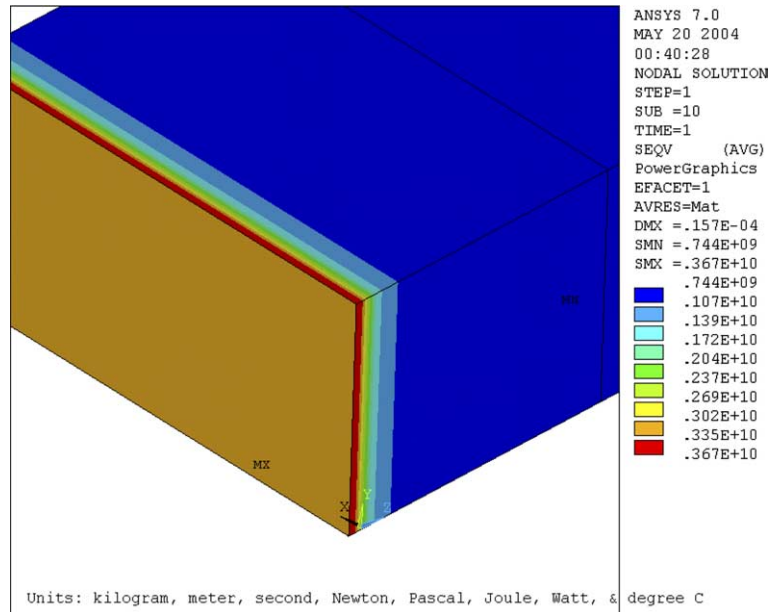


Fig. 13. Von Mises elastic stresses (Pa) in a 300 μm thick tungsten layer on top of a cooled 3-mm thick steel substrate (analysis shows stresses at the end of He-implantation 3.5e–6 s; temperature dependent material properties were used, symmetry boundary conditions were applied to all sides except for top surface and cooled bottom face).

The high stresses at the surface indicate that large plastic thermal distortions are to be expected in solid tungsten armor. Such large distortions would inevitably lead to surface cracking and failure. Fig. 2 shows an example of surface cracks resulting from rapid heating of a sintered (solid) tungsten coating on a copper substrate (e-beam: 120 keV, 10 μm penetration, 1.8 ms pulse; 2.3 MJ m^{-2} beam energy density). It is therefore critical to use a form of materials engineering to accommodate the thermal stresses. Two material engineering approaches have been presented here, plasma spray nano-porous tungsten coatings and open tungsten foams. Both need to distribute the X-ray and ion energy deposition in a quasi-volumetric fashion, and at the same time, have to expand without significant geometric constraints. In this work we address the question of how to engineer tungsten foam structures so as to alleviate large thermal stresses. Modeling efforts for plasma sprayed coatings are underway and will be reported in the future.

5.2. Thermal stresses in tungsten foam

The flexibility of the cellular foam structures allows translation and rotation of the ligaments, which relieves stress levels. Un-deformed and

deformed configurations of the foam structure at the end of the heating pulse are shown in Fig. 14. The maximum radial expansion of the foam cells is about 5 μm (towards the chamber center). These results are based on a solely elastic analysis and as such overestimate strain and displacements. However, what is interesting to note in Fig. 14 is that the foam structure allows for ligament and hence full-cell rotation. Therefore, the geometric constraints imposed on solid tungsten first wall structures are greatly removed, which reduces the overall level of thermal stress within the foam structure.

5.2.1. Transient elasto-plastic analysis

A three-dimensional transient elasto-plastic analysis was performed using a W-foam solid model. The rapid heating rates will result in very high strain rates. Estimates of strain rates caused by the high heating rates of the threat spectra X-rays and ions were not available at the time of this report. Instead, a series of experimental temperature dependent true stress strain curves for polycrystalline tungsten were identified for a range of quasi-static ($3 \times 10^{-3}/\text{s}$) and dynamic (10^3 – $4 \times 10^3/\text{s}$) strain rates [40]. Fig. 15 shows the true stress–strain behavior of the polycrystalline tungsten at a strain rate of $10^{-3}/\text{s}$ for various temperatures.

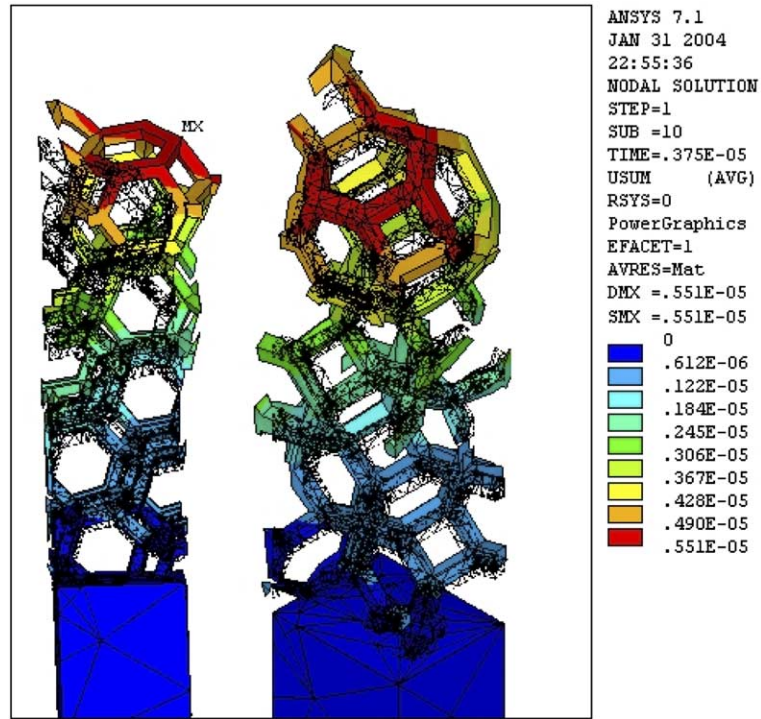


Fig. 14. Two views of deformed and un-deformed W foam armor (unconstrained section; dotted outline shows the original foam shape; displacement dimensions are in m).

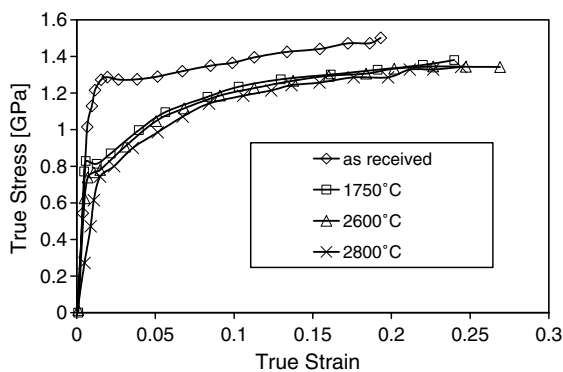


Fig. 15. Stress–strain curves for polycrystalline tungsten at quasi-static strain rates ($10^{-3}/s$) (as-received; annealed at 1750 °C, at 2600 °C, and at 2800 °C) [40].

For the transient analysis, stress strain curves at the highest available experimental strain rate ($4 \times 10^3/s$) were used [40]. A simplified cubic cell-based W-foam model was employed. Characteristic ligament dimensions of the cubic W-foam model are 25 μm thick and 125 μm long (Fig. 16). A coupled thermal and stress analysis was carried out. The model assumes symmetry boundary conditions on

all four sides of the foam. Net displacements are, therefore towards the center of the chamber. At the end of the X-ray pulse net displacements are of the order of 0.03 μm . The reason for these small displacements is that at 0.8 ns into the pulse, only 0.5 μm of the top surfaces of W-ligaments has been heated. The remainder of the tungsten material has not experienced any change in temperature at this time.

Van Mises stress distributions were calculated for a sequence of exposure times to X-rays at 0.2, 0.4, 0.6, and 1 ns. A maximum strain of 0.025 at the end of the X-ray pulse (1 ns) developed in the illuminated foam ligaments. The interesting observation is that only areas in the vicinity of illuminated ligaments experience these deformations. The foam/substrate interface strains are smaller by a factor of about 10 compared with the top ligaments. The sharp corners of the model introduced significant stress concentrations and thus stresses went well beyond the ~ 1.5 GPa maximum stress for a strain rate of $4 \times 10^3/s$ [40]. A more detailed three-dimensional transient thermo-mechanical analysis of the tungsten foam is currently being performed and results will be reported at a later time.

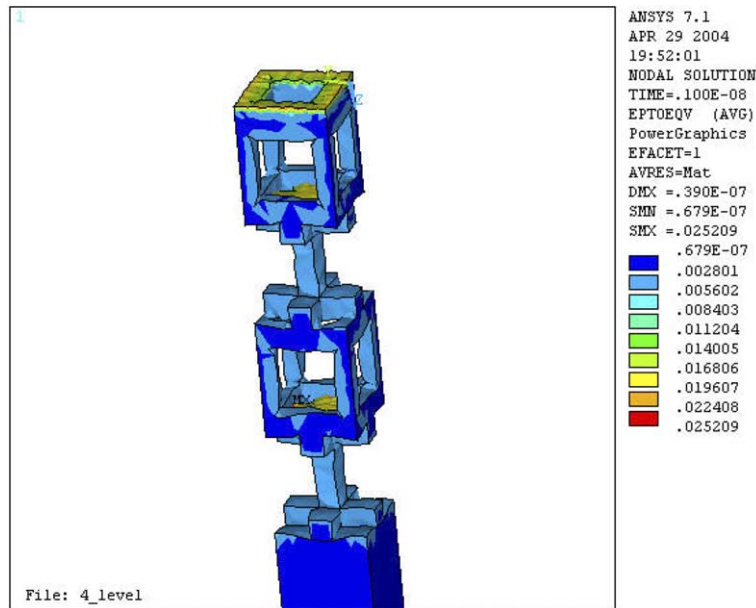


Fig. 16. Total von Mises strains at the end of the X-ray pulse (1 ns) using an elasto-plastic analysis maximum strain ~ 0.025 (display scale is 500 \times ; temperature dependent material properties were used; symmetry boundary conditions were applied to all sides except to top surface and cooled bottom face).

6. Helium management

6.1. Ion implantation damage in tungsten armor

Following the pellet explosion, energetic helium ions are implanted into the FW armor. Characteristic helium implantation ranges in solid tungsten were estimated using the SRIM-2004 Monte Carlo computer program [42]. The helium ions span an energy range from a few keV to several MeV, which results in a deposition depth starting with the surface to about 5 μm . The helium ions interact with host lattice atoms producing point defects, such as vacancies and self-interstitial atoms. These defects serve as trapping sites for the otherwise insoluble helium atoms. Continued helium implantation results in the formation and growth of helium filled bubbles. In addition to the ion generated damage, long term neutron displacement damage must also be considered. However, because the ion induced damage is so severe compared with neutron damage, neutron effects will not be considered in the current analyses.

Helium damage parameters in tungsten are given in Table 5. The severity of the large damage rates (226 dpa/s) becomes apparent when we compare them to typical damage rates in fission reactor fuel claddings or in the first wall of magnetically

confined fusion reactors, which are in the range of 10^{-7} – 10^{-6} dpa/s. During the on-time of the pulse the instantaneous helium/dpa ratio is about 2725 He/dpa. In fission and magnetic fusion systems typical He/dpa ratios are in the range of 0.1–1 He/dpa, and 10–20 He/dpa for magnetic confinement systems, respectively. Even the quasi-steady-state damage rates are several orders of magnitude larger than current experience in fission and magnetic fusion systems. For example, the average displacement damage rate for HAPL tungsten armor is 2.15×10^{-3} dpa/s, while fission damage rates are of the order of $<10^{-6}$ dpa/s. The HAPL average helium implantation rate is 5.85×10^{-6} He/at s, which is about two orders of magnitude larger than helium production rates in magnetically confined fusion reactors. If this large amount of helium is trapped in the tungsten armor, it would lead to blistering and exfoliation and rapid failure. Thus, one of the key areas of research and armor optimization is to find ways to release most if not all of the implanted helium between shots. We consider helium motion and transport next.

6.2. Helium transport and release

During the process of bubble nucleation, helium is trapped in free vacancies forming substitutional

Table 5
Tungsten damage parameters for energetic helium ions from a 154 MJ NRL target in a 6.5 m radius chamber

Parameter	Value	Units
Helium atoms per shot	1.96×10^{20}	Ions
FW solid surface area	531	m ²
Helium penetration depth	5×10^{-6}	m
Tungsten volume implanted with He	2.655×10^{-3}	m ³
Average He concentration in W per shot	7.382×10^{22}	He/m ³
Fractional He concentration in W per shot	1.17	appm
Vacancies produced per He (average)	308	Vacancy
Vacancies produced per H (average)	60	Vacancy
Displacement damage per shot	4.3×10^{-4}	dpa/shot
Pulse on-time	2.9	μs
Instantaneous damage rate	148	dpa/s
Instantaneous He implantation rate	2721	appm/dpa
Quasi-steady-state damage rate	2.15×10^{-3}	dpa/s
Quasi-steady-state He implantation rate	5.85×10^{-6}	He/at s

sites, which serve as bubble nucleation sites. These nuclei can grow into bubbles by agglomeration of vacancies and helium. Capture of vacancies by helium-vacancy clusters is a significant bubble growth mechanism. If helium implantation rates are large, the fraction of occupied vacancies, which are tied up with helium–vacancy complexes, can be quite substantial. Thus, the balance between free vacancy and interstitial fluxes arriving at bubbles can be greatly disturbed. A very high helium concentration can therefore result in very long nucleation transients of bubbles. Under these conditions, separation of distinct nucleation and growth phases may not be so clear.

The effects of helium generation on the evolution of bubbles in vanadium have been simulated using dynamic helium charging experiments and helium co-implantation during ion irradiation experiments [41,43]. Formation of voids in the absence of helium has also been extensively studied. Irradiation experiments with helium indicate the presence of at least two types of helium trapping sites for the formation of He–vacancy (HeV) clusters: (1) interstitially dissolved impurities (C, O, N) and (2) small-size precipitates and other micro-structural features, such as grain boundaries, dislocations, etc. Kinetic rate theory has been used successfully to model the experimental bubble nucleation and growth in vanadium alloys subject to helium implantation [44–46]. We introduce here an extension of our rate theory models of helium–vacancy clustering and bubble growth [46]. The model is formulated in the spirit of the mean-field approximation, to allow for relatively simple calculations of spatially average micro-structure. The model was extended to include

the effects of pulsed mode operation plus the effects of fast temperature swings during each cycle. We first present the results using only time averaged displacement damage and He/dpa rates at an average temperature of 1000 °C. The time-averaged analysis is followed by the one using transient displacement damage and helium implantation rates. Last, the effects of the rapid temperature rise and drop are included to show thermal effects on the evolution of the helium bubbles.

Following the notation of Ref. [46], the kinetic rate equations for vacancy (v), self-interstitial (i), interstitial helium (g), and substitutional helium (gv), are modified, and given as spatially homogeneous rate equations. Additional rate equations are written for small vacancy–helium clusters, containing up to three gas atoms. These equations are then used to calculate the nucleation rate of average size matrix bubbles, and hence their density. Cavities in the matrix, attached to precipitates, and on grain boundaries are treated in an average sense, in which standard growth rate equations are included. To treat the direct formation of sessile and glissile defect clusters in cascades, we included two equations for their concentrations. Details of the model will be presented in an upcoming publication.

The evolution of helium bubbles in tungsten with a quasi-steady-state implantation at an average temperature of 1000 °C is shown in Fig. 17. The damage rates are listed in Table 5. As expected the concentrations of helium bubbles increases steadily to extremely high and unrealistic values of $\sim 10^{25}$ cm⁻³ after only 1000 s of irradiation. These results indicate the severity of the challenge posed by

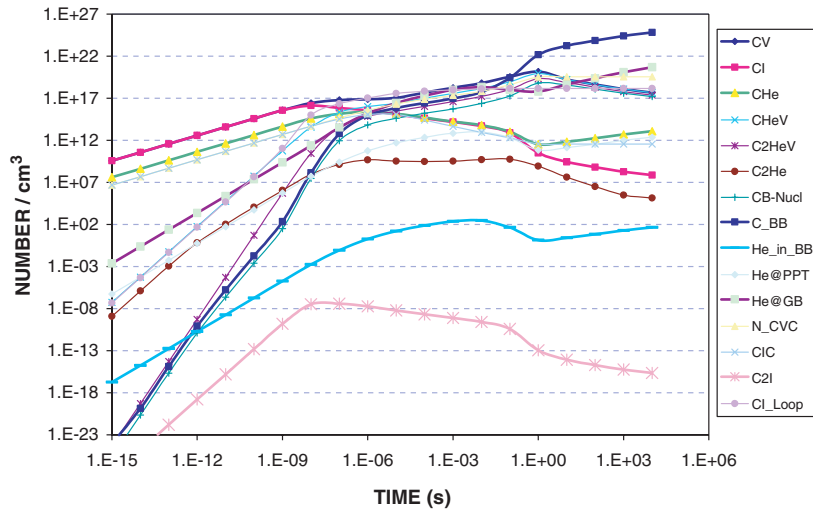


Fig. 17. Concentrations of helium–vacancy clusters and bubbles for quasi-steady state irradiation conditions (see Table 5 for damage rates).

the high helium implantation rates in IFE FW armor.

Next, we investigate the influence of radiation pulsing on the evolution of helium–vacancy clusters and bubbles in tungsten. Fig. 18 shows the evolution of cluster densities during simultaneous displacement damage and helium implantation at a constant temperature of 1000 °C. The bubble concentration reaches high levels ($\sim 10^{16}/\text{cm}^3$) within a single shot. Next, we model the effects of the temperature spike (Fig. 7), which occurs during the implantation.

The temperature of the implanted region increases rapidly during the pulse, then decays rapidly during the off time. At elevated temperatures, the stability of helium–vacancy clusters and helium bubble nuclei is reduced. Furthermore, at elevated temperatures diffusion of clusters, vacancies, and interstitials rises sharply and defect loss mechanisms offset the balance between defects. Thus, the net arrival rate of growth promoting defect fluxes can drop at elevated temperatures and bubble nucleation and growth can be impeded.

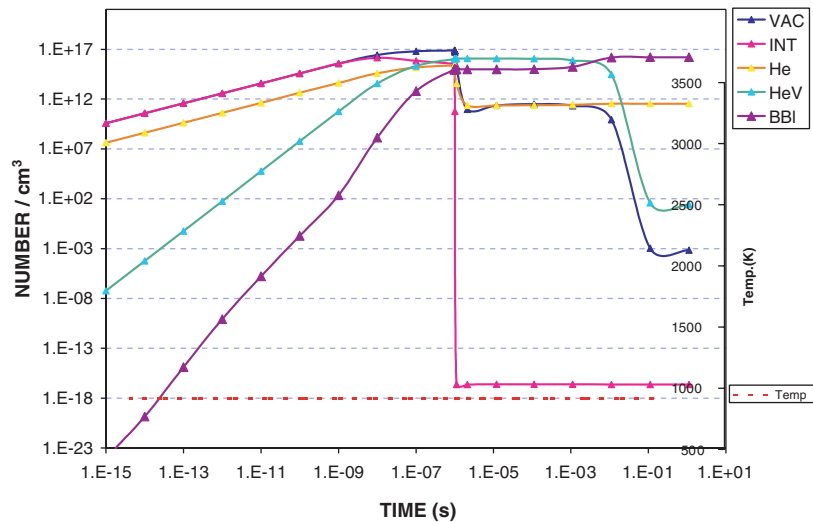


Fig. 18. Concentrations of helium–vacancy clusters and bubbles after a single pulse without temperature excursions (see Table 5 for damage rates).

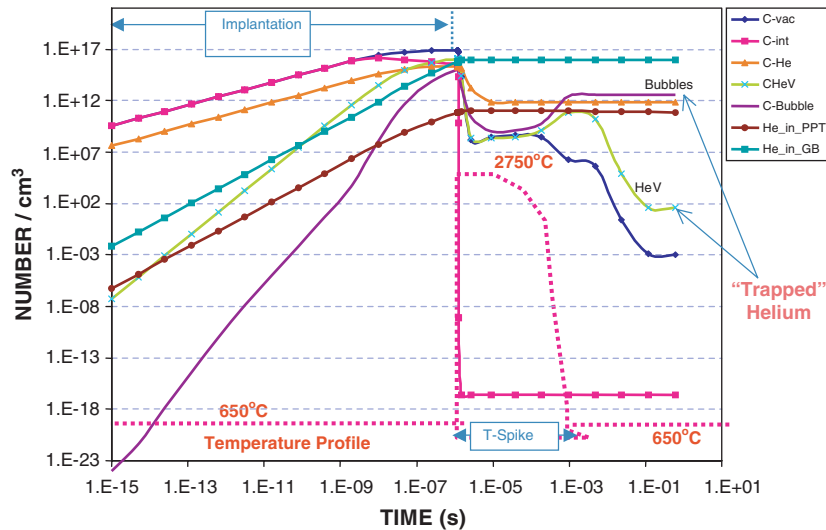


Fig. 19. Concentrations of helium–vacancy clusters and bubbles for a single pulse with superimposed temperature cycle (see Table 5 for damage parameters).

Fig. 19 shows the effects of a temperature transient during a single pulse. Helium bubble densities drop to about $10^{12}/\text{cm}^3$ or a factor of 10000 lower than at constant temperature. These results indicate that transient temperatures, pulsed implantation, and annealing during the long of-time all contribute to a significant decrease in helium bubble number densities. One of strategies to optimize the armor design can be based on maximizing the impact of the rapid temperature rise in the implanted regions.

6.3. Helium bubble kinetics during pulsed IFE operation

Two important aspects of the helium behavior are not included in the current model: (1) bubble kinetics and (2) spatial variations or the effects of armor geometry. Helium is implanted up to a depth of about $5\ \mu\text{m}$ into the W-armor. Both, the free surface and the ‘helium-free’ tungsten zone ($>5\ \mu\text{m}$) constitute sinks for mobile clusters, such as helium ions, defects clusters, and helium bubble nuclei.

The effect of bubble kinetics is significant, in that bubble migration can affect bubble growth through coalescence, which in turn results in blistering and exfoliation. A recent set of IFE relevant He implantation experiments followed by cyclic heating showed a marked increase in helium release during heat flashing [6]. Implantation with $5 \times 10^{20}\ \text{He}/\text{m}^2$ at $850\ \text{°C}$ followed by heating to $2000\ \text{°C}$ did not result in significant helium release from either single

crystal or poly-crystalline tungsten. However, implantation packets of $10^{16}\ \text{He}/\text{m}^2$ per cycle at $850\ \text{°C}$ and annealing at $2000\ \text{°C}$ in 1000 cycles to reach the same total dose of $10^{20}\ \text{He}/\text{m}^2$ in single crystal tungsten resulted in release of almost $\sim 95\%$ of the implanted helium compared to only $\sim 70\%$ released from polycrystalline tungsten. The experimental implantation depths were of the order of $1.7\ \mu\text{m}$, which results in a helium concentration of about $5 \times 10^{15}\ \text{He}/\text{cm}^3$ per shot for a $10^{16}\ \text{He}/\text{m}^2$ per cycle dose. These concentrations are close to the helium concentration estimated for HAPL IFE conditions: $7.382 \times 10^{16}\ \text{He}/\text{cm}^3$ per shot (Table 5).

Surface blistering of polycrystalline tungsten samples occurred at helium doses greater than or equal to $10^{21}\ \text{He}/\text{m}^2$ ($\sim 5 \times 10^{20}\ \text{He}/\text{cm}^3$ assuming $2\ \mu\text{m}$ deposition depth), which corresponds to a peak helium concentration of $\sim 0.7\ \text{at.}\%$. Helium doses that resulted in surface blistering ranged between $10^{21}\ \text{He}/\text{m}^2$ and $10^{22}\ \text{He}/\text{m}^2$. For a $6.5\ \text{m}$ radius HAPL IFE chamber the maximum He-implantation rates are of the order of $10^{16}\ \text{He}/\text{m}^2$, which are close to some of the experimental implantation rates reported in Ref. [6]. Under these conditions blistering is avoided due to release of more than 95% of the helium during the heating cycles. The flash heating/cooling cycle durations are $\sim 18\ \text{s}$, which are much longer than HAPL IFE heating/cooling cycles of a few ms. The experimental heating cycles are too long to reflect the full impact

of rapid temperature swings on helium bubble evolution. Rate-theory based models are being developed to model the helium bubble kinetics during these rapid transients, which will be published in future.

7. Optimization of micro-engineered tungsten armor

Micro-engineered armor is being considered as candidate materials to accommodate the high loading conditions of an IFE FW. Two concepts have been identified as promising, nano-porous plasma sprayed tungsten and open cell tungsten foam. These concepts will require significant research and development before a reliable armor can be designed.

7.1. Optimizing plasma sprayed nano-porous tungsten

Advanced nano-porous plasma spray deposited tungsten has been shown to be permeable to helium gas while having a relatively high thermal conductivity (~ 110 W/m K at room temperature). Furthermore, the characteristic dimensions of the nano-porous tungsten are of the order of helium bubble migration distances observed in flash heated helium implantation experiments [6]. Although, it should be noted that the experimental flash heating cycle of about 18 s is much longer than the heating cycle in IFE (< 1 ms).

The nano-sized plasma sprayed ‘splats’ are stabilized against grain growth by addition of HfC. The plasma spray process results in a network of ‘loosely’ bonded solidified splats. Under high heat loads, these bonds are subject to significant stresses, which can result in failure and significant release of material. The primary challenge is to develop splat-to-splat bonding strengths that can withstand the high cycle heating rates of IFE.

The nano-porous tungsten maintains an as deposited sub-micron grain structure because of the addition of HfC. The HfC ($< 0.3\%$) serves as a grain growth inhibitor. Addition of 0.32% HfC to W–4Re alloys has been shown to increase the strength and decrease creep rates [48] significantly. The HfC containing tungsten is therefore less tough (more brittle) than a pure tungsten metal. The need for sufficient toughness to withstand thermal shocks and vibrations during operation for the armor is critical. Increased toughness will be one of the optimization criteria for nano-porous plasma sprayed armor.

7.2. Optimizing tungsten foam armor

The advantage of tungsten foam is the open structure, which can accommodate significant deformations prior to failure. Foam structures have very large surface area per unit volume. These internal areas could accommodate helium recycling. However, the state-of-the art tungsten foam has several research and development challenges, which need to be met for reliable operation in an IFE environment. These fall under three categories (1) foam and ligament dimensions, (2) ligament core materials, and (3) ligament surface features.

Tungsten foams are currently manufactured containing a 20 μm thick carbon core and a tungsten coating of about 30–50 μm . The total ligament diameter is above 100 μm . For the IFE armor applications, the ligament diameter needs to be reduced to less than 20 μm in order to obtain more uniform heating of individual ligaments. Ligament diameters also determine the foam pores per inch density (ppi). The current state of the art tungsten foams have a pore density of less than 100 ppi. This density is too low for IFE applications, because lower pore densities require thicker foams to fully shield the underlying structure from radiation. The armor thickness needs to be kept as small as possible to minimize the tortuous conduction path to the cooled substrate.

The core of the tungsten ligaments consists of carbon, which can react with tungsten to form WC at high temperatures. Compared with pure tungsten, WC has much lower toughness, lower thermal conductivity (84 W/m K at $T = 20$ °C [49]) and a lower melting temperature (2900 °C). The carbon core has to be either removed or replaced with more stable carbides, such as TaC or HfC. Tungsten foams having TaC or HfC cores have recently been manufactured and are being tested in the Sandia National Laboratory RHEEP facility [9].

It is well known that implanted helium migrates rapidly to grain boundaries, where it accumulates to form grain boundary helium bubbles. A significant helium release rate may be achieved if the surface of the foam ligaments were decorated with individual single tungsten crystals. These crystals would have to have characteristic dimensions similar to the implantation depths of about 5 μm . Recently, tungsten foam coated with crystal felt has been manufactured [47]. Fig. 20 shows an SEM of ‘nano-turf’ coated tungsten foam: the ligaments are coated with single tungsten crystals

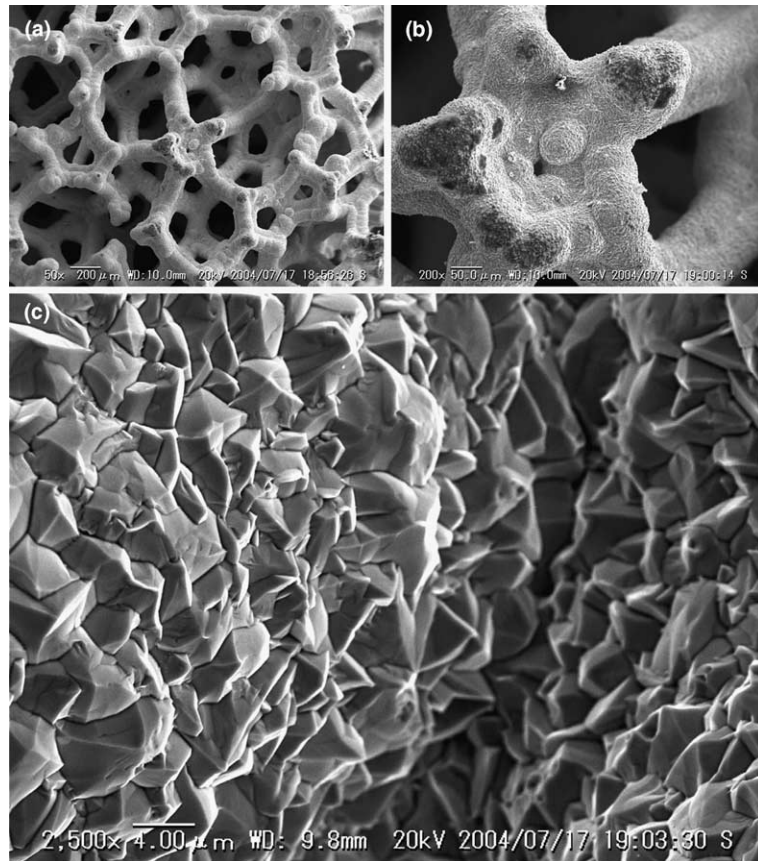


Fig. 20. 'Nano-turf' coated tungsten foam; (a) 50×; (b) 200×; (c) 2500× magnification; the ligaments are coated with single tungsten crystals having characteristic lengths scales of the order of 5 μm.

having characteristic lengths scales of the order of 5 μm, which is the maximum helium penetration dept).

Although, many challenges lay ahead, preliminary investigations of micro-engineered FW armor indicate these materials offer potential venues to accommodate the cyclic high temperature and ion implantation operation of an IFE device.

8. Summary and conclusions

The HAPL program is developing inertial fusion energy engineering test facility with a solid first wall chamber. Tungsten has been identified as the candidate armor material to protect the low activation ferritic first wall. The challenges in developing viable tungsten armor can be divided into three major categories: (1) bonding to the steel substrate, (2) thermo-mechanical response to rapid and high temperature cyclic loads, and (3) recycling of the large implanted helium dose.

The large almost instantaneous heating ($\sim 2 \times 10^{16}$ W/cm³, $\Delta t \sim 2$ μs) and the large ion implantation rates ($\sim 7 \times 10^{16}$ He/cm³ per shot) could result in early failure and unacceptable material loss due to blistering and exfoliation. To accommodate these loads at a repetition rate of 5 Hz, micro-engineered materials are suggested. Preliminary assessment of two micro-engineered materials, nano-porous plasma sprayed tungsten and open cell tungsten foam were conducted.

Using HfC (<0.3%) as grain growth inhibitors plasma sprayed nano-porous tungsten coatings with stable sub-micron (~ 0.5 μm) grain structures, high helium gas permeability ($\sim 10^{-3}$ Torr cm³/s), and high thermal conductivity (~ 110 W/m K) have been manufactured. The high interconnected sub-micron porosity can facilitate large helium recycling rates. Tungsten foams with pore densities of 100 ppi (pores per inch) have been manufactured. The open cell structure of foams transforms the high surface loads into 'quasi-volumetric' heat loads.

Thermo-mechanical analysis shows that thermal stresses can be reacted by the rotation and deformation of the foam ligaments. Helium implantation experiments in solid tungsten at doses of $\sim 10^{16}$ He/cm³ per shot followed by heat flashing at 2000 °C showed a significant release of $\sim 95\%$ of helium from single crystal and $\sim 70\%$ from polycrystal tungsten. Although experimental flash heating cycles were too long (~ 18 s) compared with HAPL conditions (~ 3 ms), the high helium release rates indicate significant helium recycling due to high temperature cyclic operation.

Because IFE relevant irradiation conditions cannot be achieved experimentally, a detailed kinetic rate theory model was developed to study helium transport during pulsed operation. The model showed a factor of 10000 drop in bubble concentration per shot due to the large temperature spike in the implantation zone (~ 5 μm , ~ 2800 °C, $\Delta t \sim 2$ μs).

Preliminary assessment of micro-engineered materials has identified several optimization directions for micro-engineered nano-porous and tungsten foam structures. Addition of grain growth inhibitors, such as HfC (0.32%) has been shown to decrease the toughness in W-4Re alloys. An increase in toughness of the plasma sprayed nano-porous tungsten might be critical to survive thermal shocks and vibrations. Furthermore, the ‘weak’ bonds between re-solidified tungsten splats in a plasma sprayed coatings may not survive the intense radiation loads of IFE. Future research and development has to focus on increasing bond strength without inducing significant sintering or pore closure in nano-porous tungsten.

The tungsten foam faces several research and development challenges. Foremost is the development of refractory foams with much smaller ligament dimensions and much higher pore densities. Ligament sizes need to shrink from hundreds of microns to less than 20 μm and pore densities need to increase from 100 ppi to more than 300 ppi. Next the carbon core of refractory foam ligaments needs to be replaced by stable carbides, which will not react with tungsten. Finally, the helium implantation depth is of the order of 5 μm , which necessitates characteristic ligament surface features having similar dimensions.

Although the challenges in developing a viable solid FW armor are enormous, preliminary assessment of micro-engineered tungsten armor has shown that these materials offer potential solutions to many of the IFE operational challenges.

Acknowledgments

Numerous individuals and institutions have contributed to this work. Although their specific work and contribution may not be cited in this publication, the authors wish to thank everyone for their input. This work is sponsored by the US Department of Energy, NNSA/DP.

References

- [1] J.D. Sethian et al., Nucl. Fusion 43 (2003) 1693.
- [2] L.S. Lance et al., J. Nucl. Mater., these Proceedings.
- [3] J.W. Davis, V.R. Barabash, A. Makhankov, L. Ploch, K.T. Slattery, J. Nucl. Mater. 258–263 (1998) 308.
- [4] Tivey et al., ITER divertor design issues and research and development, SOFT-20, 1998, p. 207.
- [5] R.E. Nygren, D.L. Youchison, R.D. Watson, S. O’Dell, Fusion Eng. Des. 49&50 (2000) 303.
- [6] S.B. Gilliam, S.M. Gidcuma, N.R. Parikh, B.K. Patnaik, J.D. Hunn, L.L. Snead, G.P. Lamaze, J. Nucl. Mater., these Proceedings, doi:10.1016/j.jnucmat.2005.08.017.
- [7] L. Snead, HAPL Workshop, University of California at San Diego, San Diego, CA, 4–5 April 2002.
- [8] J. Kulcinski et al., HAPL Workshop, Georgia Institute of Technology, Atlanta, Georgia, 5–6 February 2004.
- [9] T. Renk, High Average Power Laser Workshop, Madison, WI, 24–25 September 2003.
- [10] S. Odell, Engineered Tungsten Armor, private communications, April 2004.
- [11] J. Linke, T. Hirai, M. Rödiger, L. Singheiser, 14th International Stellarator Workshop, Greifswald, Germany, 22–26 September 2003.
- [12] T. Hirai, J. Nucl. Mater. 313–316 (2003) 67.
- [13] T. Tanabe et al., J. Nucl. Mater. 241–243 (1997) 1164.
- [14] M. Wada et al., J. Nucl. Mater. 241–243 (1997) 799.
- [15] R.E. Nygren, D.L. Youchison, R.D. Watson, S. O’Dell, Fusion Eng. Des. 49&50 (2000) 303.
- [16] Y. Arata, A. Kobayashi, Y. Habara Transactions of the Joining and Welding Research Institute JWRI, vol. 15, Osaka University, Osaka, Japan, 1986, p. 227.
- [17] A. Kobayashi, S. Sharafat, N. Ghoniem, Surf. Coat. Technol., 2005 (draft available on line).
- [18] MRS Bulletin, in: Lorna J. Gibson (Guest editor), Cellular Solids, April 2003.
- [19] G. Reyes Villanueva, W.J. Cantwell, Compos. Sci. Technol. 63 (2003) 1-S20.
- [20] M.F. Ashby, A.G. Evans, N.A. Fleck, L.J. Gibson, J.W. Hutchinson, H.N.G. Wadley, Metal Foams, A Design Guide, Butterworth-Heinemann, 2000.
- [21] L.J. Gibson, M.F. Ashby, Cellular Solids: Structure and Properties, 2nd Ed., Cambridge University, Cambridge, 1999.
- [22] Proceedings of the 3rd International Conference on Cellular Metals and Metal Foaming Technology (MetFoam 2003), Berlin (Germany), 23–25 June 2003.
- [23] J. Klett, R. Hardy, E. Romine, C. Walls, T. Burchell, Carbon 38 (2000) 953.
- [24] A. Sherman, B. Williams, M. DelaRosa, La Ferla, in: MRS Symposium Proceedings – Mechanical Properties of Porous

- and Cellular Materials, vol. 207, Pittsburgh, PA, 1990, p. 141.
- [25] B. Williams, Manufacturing processes for tungsten foam at Ultramet Inc., Los Angeles, CA, private communications, June 2003.
- [26] R.F. Radel, Kulcinski, 10th High Average Power Laser Program Workshop, Princeton Plasma Physics Laboratory, Princeton, NJ, 27–28 October 2004.
- [27] A.R. Raffray, L. El-Guebaly, G. Federici, D. Haynes, F. Najmabadi, D. Petti/Aries-IFE Team, Fusion Sci. Technol. 46 (3) (2004) 417.
- [28] N. Ghoniem, Kulcinski, Nucl. Technol. Fusion 2 (2) (1982) 165.
- [29] N. Ghoniem, A. El-Azab, Fusion Eng. Des. 29 (1995) 89.
- [30] A. El-Azab, N. Ghoniem, Fusion Eng. Des. 27 (1995) 536.
- [31] E.G. Lovell, R. Peterson, R. Engelstad, G. Moses, UWFD-421, Also The Second Topical Meeting on Fusion Reactor Materials, Seattle, WA, 1981.
- [32] J. Latkowski, Issues and Activities for Issues and Activities for Laser-IFE Optics, Snowmass, CO, 10 July 2002.
- [33] Raffray et al., J. Nucl. Mater., these Proceedings, doi:10.1016/j.jnucmat.2005.08.015.
- [34] J. Blanchard, HAPL Meeting at Naval Research Laboratories, Washington, DC, 2–3 December 2002.
- [35] A.F. Mills, Basic Heat and Mass Transfer, Prentice Hall, 1998.
- [36] S. Zinkle, J. Robertson, R. Klueh, Fusion Materials Semi-annual Progress Report for Period Ending June 30, 1998, DOE/ER-0313/24, ORNL, TN, 1998, p. 135.
- [37] S. Zinkle, S. Majumdar, N.M. Ghoniem, S. Sharafat, APEX Interim Report, University of California Los Angeles, Los Angeles, CA, 1999, p. 13.1.
- [38] S. Sharafat, M. Andersen, Q. Hu, N. Ghoniem, High Average Power Laser Program Workshop, University of Wisconsin, MA, 24–25 September 2003.
- [39] J. Davis, ITER Material Database Handbook, Boeing Company, Available from: <<http://aries.ucsd.edu/LIB/PROPS/ITER/>>.
- [40] T. Dummer, J.C. Lasalvia, G. Ravichandran, M.A. Meyers, Acta Mater. 46 (17) (1998) 6267.
- [41] Dale L. Smith, H. Matsu, J. Nucl. Mater. 307–311 (Part 2) (2002) 1488.
- [42] J.F. Ziegler, SRIM-2003, The Stopping and Range of Ions in Matter, Available from: <<http://www.srim.org/>>.
- [43] N. Sekimura, Y. Shirao, H. Yamaguchi, S. Yonamine, Y. Arai, J. Nucl. Mater. 271&272 (May) (1999) 63.
- [44] S. Sharafat, N. Ghoniem, J. Nucl. Mater. 122 (1–3) (1984) 531.
- [45] N. Ghoniem, J. Alhajji, D. Kaletta, J. Nucl. Mater. 136 (2–3) (1985) 192.
- [46] S. Sharafat, N. Ghoniem, J. Nucl. Mater. 283–287 (Part 2) (2000) 789.
- [47] B. Williams, Ultramet Inc. Pacoima, CA, private communications, August 2004.
- [48] J. Park, Mater. Sci. Eng. A 265 (1999) 174.
- [49] CRC Materials Science and Engineering Handbook, CRC Press, p. 279.